• U C •

FCTUC FACULDADE DE CIÊNCIAS
E TECNOLOGIA
UNIVERSIDADE DE COIMBRA

DEPARTAMENTO DE
ENGENHARIA MECÂNICA

Simulação Numérica do Processo de Estampagem de Placas Bipolares Metálicas

Dissertação apresentada para a obtenção do grau de Mestre em Engenharia Mecânica na Especialidade de Produção e Projeto

Numerical Simulation of the Stamping Process of Metallic Bipolar Plates

Autor
Nicolas Marques

Orientador
Diogo Mariano Simões Neto

Júri

Presidente	**Professor Doutor Luís Filipe Martins Menezes** **Professor Catedrático da Universidade de Coimbra**
Vogal	**Professora Doutora Marta Cristina Cardoso de Oliveira** **Professora Auxiliar da Universidade de Coimbra**
Orientador	**Professor Doutor Diogo Mariano Simões Neto** **Professor Convidado da Universidade de Coimbra**

Coimbra, Julho, 2016

“I never lose, I either win or learn”

Unknown.

Acknowledgments

This work as well as my engineering degree would not be possible without the help and support of my family, my friends and the teachers who supported me through this educational path.

First and foremost, I want to express my gratitude to my scientific advisor Professor Diogo Mariano Simões Neto for all the support and guidance during this work. It has been a privilege to work with a professor with such dedication to his students and insightful suggestions. Thank you for the knowledge transmitted during this work as well as the sincere friendship. I am also grateful for the help from Professor Marta Cristina Oliveira Cardoso and Professor Luís Filipe Martins Menezes on some difficulties encountered in this work.

Secondly, I want to thank especially my good friend Mariana Moura for putting up with me for all these years of my mechanical engineering degree, always helping me when needed and for being by my side. Her tips and suggestions for this work have the most deserved recognition. I greatly appreciate the encouragement and friendship.

I would like to thank my friend António Camilo for proofreading and providing me with helpful feedback on this work. I want to thank for the continued friendship.

I want to thank my colleagues and friends from all these years, namely Hugo Matos, André Brás, Diana Almeida, André Travassos, Vânia Sousa, Diogo da Silva and Francisco Brito. To my friend Adrian de Francisco back in Switzerland for never forgetting me and always keeping in touch, I want to thank for all the good memories back in the days.

Finally, I want to thank my family for their unconditional love and support, namely my parents without whom this life would never be possible and for always believing in me all these years. A huge thanks to my godparents and cousin back in Switzerland for always encouraging me and for all the support along all these years.

This work was carried out under the project “Improving the manufacturing of metallic bipolar plates for fuel cells using the rubber forming process” with reference PTDC/EMS-TEC/0702/2014, co-funded by the Foundation for Science and Technology and the EU/FEDER, through the program COMPETE2020 with reference POCI-01-0145-FEDER-016779.

Resumo

Uma placa bipolar é um dos principais componentes de uma célula de combustível, que é considerada como uma fonte de energia com elevado potencial para transporte e aplicações portáteis.

O principal objetivo deste trabalho é a otimização do processo de estampagem de placas bipolares metálicas, usando simulações numéricas do processo de conformação. As simulações numéricas apresentadas neste estudo foram realizadas com o programa de elementos finitos DD3IMP.

A geometria do canal de escoamento tem uma grande influência sobre a formabilidade obtida durante o processo de estampagem. Sendo assim, o objectivo deste trabalho é o de estudar as diferentes variáveis geométricas, a fim de optimizar as dimensões do canal de escoamento. Deste modo, é criado um modelo paramétrico em CAD contendo a geometria das ferramentas de estampagem, que é posteriormente utilizado na simulação numérica com o método dos elementos finitos. Devido à grande complexidade geométrica de uma placa bipolar, são criados modelos simplificados, de diferentes zonas representativas. Cada zona representativa destina-se a estudar uma região diferente da placa bipolar. cobrindo todo o comportamento de deformação encontrado na placa. Assim, é utilizada uma simples análise 2D para avaliar a secção transversal do canal da placa bipolar, enquanto que é necessária uma análise 3D para estudar a secção curva do canal de escoamento. Em seguida, é estudado o material da chapa com uma comparação entre três ligas diferentes, SS 304, Al 5042 e Al 1235. Uma vez que o processo de estampagem influencia os resultados obtidos para a conformabilidade da chapa, é realizado um estudo entre microestampagem e hidroconformação.

Os resultados numéricos mostram que o aumento do raio principal, da largura do canal e a diminuição da profundidade do canal, do raio de curvatura do raio adicionado e da secção plana do canal, a formabilidade da chapa é melhorada. As áreas críticas das placas metálicas estampadas correspondem às zonas de curvatura dos canais de escoamento sobre o raio correspondente. Tanto o aço inoxidável SS 304 como a liga de alumínio Al 1235

demonstram boa formabilidade e o processo microestampagem tem um melhor resultado em comparação com a hidroconformação.

Palavras-chave: Células de Combustível, Modelo de Elementos Finitos, Placa Bipolar Metálica, Microestampagem e Hidrocomformação, Optimização de Geometria.

Abstract

A bipolar plate is one of the key components of proton exchange membrane fuel cells, which are considered as potential power sources for transportation and portable applications.

The main objective of this work is the optimization of the stamping process of metallic bipolar plates, using the finite element simulation of the forming process. The numerical simulations presented in this study were carried out with the in-house finite element code DD3IMP.

The geometry of the flow channel has a large influence on the formability during the stamping process. Therefore, the aim of the study is to study the different geometrical variables in order to optimize the flow channel dimensions. Accordingly, a parametric CAD model containing the stamping tools' geometry is created, which is posteriorly used in the simulation with the finite element method. Due to the large complexity of a bipolar plate, a simplified model with different representative zones is created. Each representative zone aims to study a different region of the bipolar plate. covering the entire deformation behaviour found in the plate. Thus, a simple 2D analysis is used to evaluate the straight channel section of the bipolar plate, while a 3D analysis is required to study the curved section of the flow channel. Afterwards, the material of the blank is studied with a comparison between three different alloys, SS 304, Al 5042 and Al 1235. Since the stamping process influences the results obtained for the formability of the blank, a study between microstamping and hydroforming is performed.

The numerical results shown that increasing the main radius, the channel width and the rib width and diminishing the channel depth, the fillet radius and the flat section the formability of the blank is improved. The critical areas of the stamped metallic plates are on the curved flow channels on the correspondent fillet radius. Both the stainless steel SS 304 and the aluminium alloy Al 1235 demonstrate good formability and the microstamping process has an improved result compared with hydroforming in terms of formability.

Keywords PEM Fuel Cell, Finite Element Model, Metallic Bipolar Plate, Flow Channel, Microstamping and Hydroforming, Geometry Optimization.

Table of Contents

LIST OF FIGURES

LIST OF TABLES

SYMBOLS AND ACRONYMS

Variables and Symbols

h – Channel depth

E – Young's Modulus

R – Fillet radius

Y, ε_0, $\bar{\varepsilon}^{\mathrm{p}}$, K, n – Constitutive parameter of Swift's hardening law

Y, Y_0, $\mathrm{C_y}$, Y_{sat} – Constitutive parameter of Voce's hardening law

r – Main radius

s – Rib width

t – Blank thickness

w – Channel width

α – Draft angle

ν – Poisson's ratio

Acronyms

2D – Two Dimensional

3D – Three Dimensional

AFC – Alkaline Fuel Cells

Al – Aluminum

BPP – Bipolar Plate

CAD – Computer Aided Design

DD3IMP – Deep Drawing 3D IMPlicit finite element code

FE – Finite Element

IGES – Initial Graphics Exchange Specification

MCFC – Molten Carbonate Fuel Cells

PAFC – Phosphoric Acid Fuel Cells

PEM – Polymer Electrolyte Membrane

SOFC – Solid Oxide Fuel Cells

SS – Stainless Steel

1. INTRODUCTION

In the last decades there has been an increasing concern about environmental consequences on the use of fossil fuel for electricity production and vehicle propulsion. The dependence on oil became apparent during oil crises, but more importantly is the increase in global awareness of environmental consequences. Sustainable energy became important with the increase in population since common sources of energy have poisonous emissions into the atmosphere (Carrette et al., 2001).

In order to reduce the dependence on fossil fuels and diminish poisonous emissions, renewable energy from wind, water and sun are already implemented. Nevertheless, these sources are irregularly available, thus not being suited to cover all electrical needs (Carrette et al., 2001).

An option for future power generations are fuel cells, which use pure hydrogen and produce only water, eliminating all local emissions. Fuel cells have higher electrical efficiencies compared to heat engines and in combination with renewable energy it may be suited for sustainable energy generation (Carrette et al., 2001).

Fuel cells are dated to as long as 1839 but no practical use was found until the 1950s (Wang et al., 2011).

1.1. Fuel Cells

Fuel cells are electrochemical devices that convert chemical energy stored in fuels into electrical energy. The attention on this technology is mainly due to their high efficiency (60% in electrical energy conversion) and low emissions, which are interesting for transportation and portable applications (Mahabunphachai et al., 2010). The fuel cells can be categorised in five main categories: polymer electrolyte membrane (PEM) fuel cells, solid oxide fuel cells (SOFC), alkaline fuel cells (AFC), phosphoric acid fuel cells (PAFC) and molten carbonate fuel cells (MCFC). For transportation and portable applications, PEM fuel cells are promising candidates since they gather the most important characteristics for such applications (Wang et al., 2011).

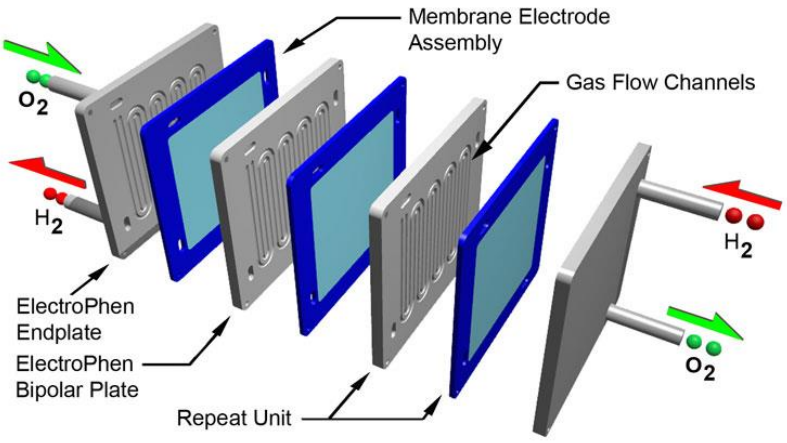

Figure 1.1. Proton exchange membrane fuel cell (PEMFC) assembly (Mahabunphachai et al., 2010).

Fuel cells are composed by different components assembled in stacks as shown in Figure 1.1. Each PEMFC stack consists of a membrane electrode assembly and bipolar plates (Peng et al., 2014). As shown in Figure 1.2, hydrogen gas enters in contact with the anode where it is adsorbed onto the catalyst surface. Each hydrogen atom then loses an electron which flows to the cathode as current through an external circuit. The remaining hydrogen protons flow across de membrane towards the cathode where they enter in contact with air, which is previously fed to the fuel cell, and the initial electrons to form water, which is then forced to exit the fuel cell (Holton and Stevenson, 2013). The membranes on PEM fuel cells are made notably in Nafion® (Wang et al. 2011).

Although fuel cells look promising, the commercialization is still restricted due to the high cost compared with other sources of energy such as internal combustion engines. Comparing the prices of these two forms of energy, the fuel cell power is still 4-10 times more expensive as compared to internal combustion engines. The cost of fuel cells is around $200-300 per kW while other regular engines cost around $30-50 per kW. Since the bipolar plates on the fuel cells represent around 35-45% of their cost, it becomes important to have the price reduced on such plates to improve the commercialization of this technology (Mahabunphachai et al., 2010).

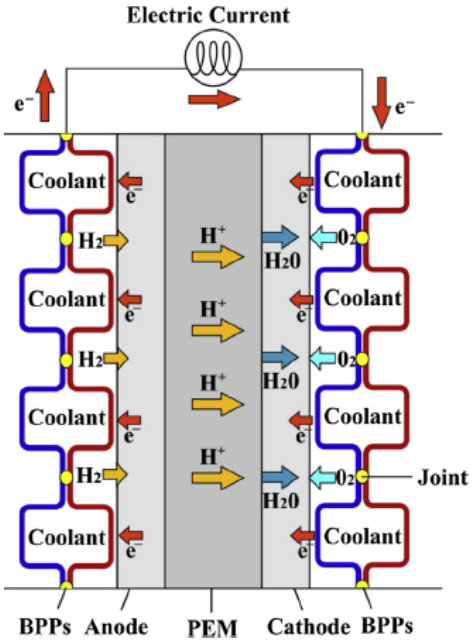

Figure 1.2. Schematic of a PEM fuel cell (Peng et al., 2014).

1.2. Bipolar Plates

Bipolar plates have an important role on fuel cell stacks. They provide structural support for the mechanically weak membranes, manage the supply of reactant gases trough flow channels (see Figure 1.3), improve heat management with a coolant and electrically connect two cells together in the stack (Peng et al., 2014).

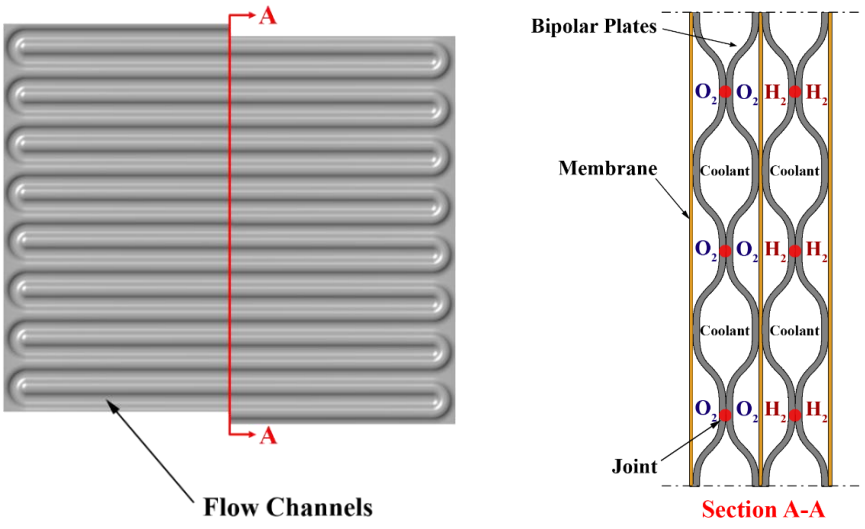

(a) (b)

Figure 1.3. Structure of a bipolar plate (a) Top view, (b) Cross Section A-A.

The configuration presented in Figure 1.3 consists of two metallic plates welded together creating the bipolar plate. This configuration repeats along the stack. The reactants flow on one side of the plate while the cooling fluid flows on the other side of the same plate to remove the heat generated by the chemical reaction (Li and Sabir, 2005).

Many materials can be used for manufacturing bipolar plates such as graphite, stainless steel, aluminium and titanium. However, for portable applications, metallic plates are preferred due to a much superior manufacturability and higher mechanical strength (Peng et al., 2014). This topic will be reviewed in depth on section 2.2. The conventional manufacturing processes used for graphite cannot be applied in metallic bipolar plates. Forming processes such as microstamping, hydroforming and rubber pad forming are more adequate to such plates and will be discussed on section 2.3 (Peng et al., 2014).

1.3. Objectives of the Study and Outline

The main objective of this study is to optimize the stamping process used to manufacture metallic bipolar plates. The finite element method is adopted to perform the numerical simulations of the forming process, requiring the development of several models. First, the preliminary results are compared with previous studies of other authors in order to validate the numerical model. The optimization of the tool's geometry demands a parametric model able to easily create the finite element model for each geometry. Then, the influence of the different geometrical parameters of the channel are analysed, namely the channel depth, rib and channel width, fillet radius and the blank's initial thickness. Besides, the behaviour of different materials is evaluated regarding its utilization in the manufacture of bipolar plates. Finally, the comparison between stamping and hydroforming is performed to verify the influence of the forming process on the formability.

This dissertation is organized into four main chapters. For a better understanding and to improve the readability, this section briefly summarizes the content on each chapter.

Chapter 1 presents the introduction on the subject of the study with a brief description of different existing fuel cells and the basic chemical functioning. The importance of the bipolar plates and the requirements for portable applications are explained, highlighting further improvements required for an effective commercialization. Thus defining the objectives for this dissertation.

Chapter 2 summarizes the study on metallic bipolar plates achieved on recent years with a main focus on the flow field design, the materials used and the most used forming processes. It presents a summary on different channel dimensions previously used, either for mechanical or chemical optimization.

Chapter 3 presents the numerical study concerning the forming of bipolar plates, considering different tool geometries, materials for the plate and forming processes. The finite element model is described along with every step of the process from tool's creation, finite element mesh generation to the simulation itself. The materials used are described with a focus on aluminium and stainless steel. The boundary conditions adopted are described as well as the number of finite elements required for accurate simulation results. Each parameter of the tool's geometry is studied individually to evaluate their influence and a comparison between different forming processes is performed. The results obtained for this study are briefly compared with previous studies to evaluate the performance of the optimized geometry.

Chapter 4 contains the main conclusions withdrawn from the study presented on previous chapters.

2. REVIEW ON METALLIC BIPOLAR PLATES

This section contains a review about the metallic bipolar plates used in fuel cells, focusing in the recent progresses in terms of flow field design, materials and different manufacturing processes.

For the last 20 years, metallic bipolar plates have been developed and experienced, but improvements have yet to be made for successful commercialization (Peng et al., 2014).

2.1. Flow Field Design

The function of the flow channels in the fuel cells is to provide reactant gases to the electrolytic membrane and to provide cooling to the fuel cell through a cooling fluid. Several flow field designs have been studied and improved for traditional graphite bipolar plates but most of them cannot be applied to stamped metallic plates. For metallic bipolar plates there are four main types of flow field designs (Peng et al., 2014):

1. Pin-type flow field,
2. Series-parallel flow field,
3. Serpentine flow field,
4. Interdigitated flow field.

(a) (b)

Figure 2.1. Pin-type flow field: (a) Schematic diagram, (b) Results from experimental hydroforming (Belali-Owsia et al., 2014).

The pin-type flow field consists of multiple pins along the plate arranged in a regular pattern. These pins can present a cubic or rounded shape as shown in Figure 2.1. This flow field is considered to achieve the best results according to the principle of least resistance regarding the reactant gases flow. However, it leads to an inhomogeneous gas distribution along the plate and can have an insufficient product water removal. This flow field is best used for high reactant flows but with lower utilization levels of fuel and oxygen (A.Heinzzel et al. 2009).

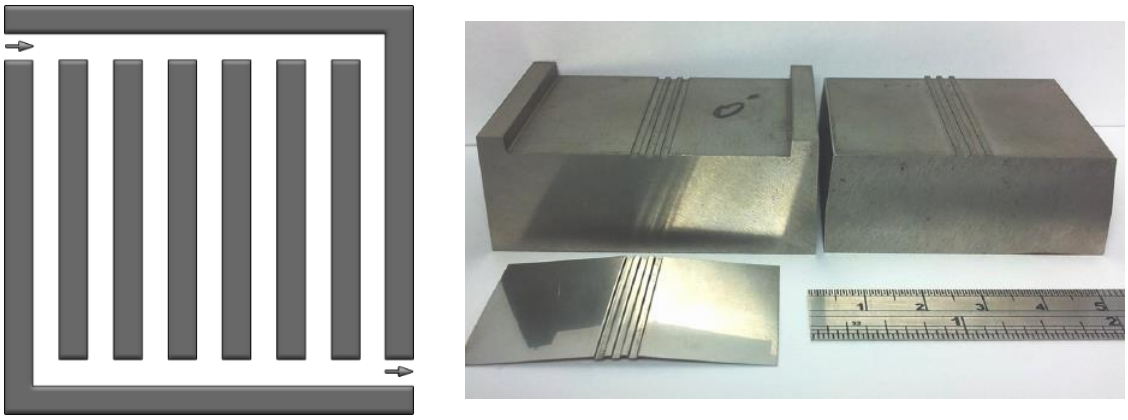

(a) (b)

Figure 2.2. Series-parallel flow field: (a) Schematic diagram, (b) stamping die set and sheet (Zhou and Chen, 2015).

Parallel flow fields (see pattern in Figure 2.2) can be used when there is no accumulation of water droplets. If droplets are formed, some channels may become blocked and the remaining gas will flow through the remaining channels creating an uneven gas distribution (A.Heinzzel et al. 2009).

Regarding the stamping process of the metallic sheets with this kind of geometry, straight channels can originate excessive springback after stamping, as shown in Figure 2.2 (b). In order to avoid this defect, wavelike flow fields can be applied, which are presented in see Figure 2.3.

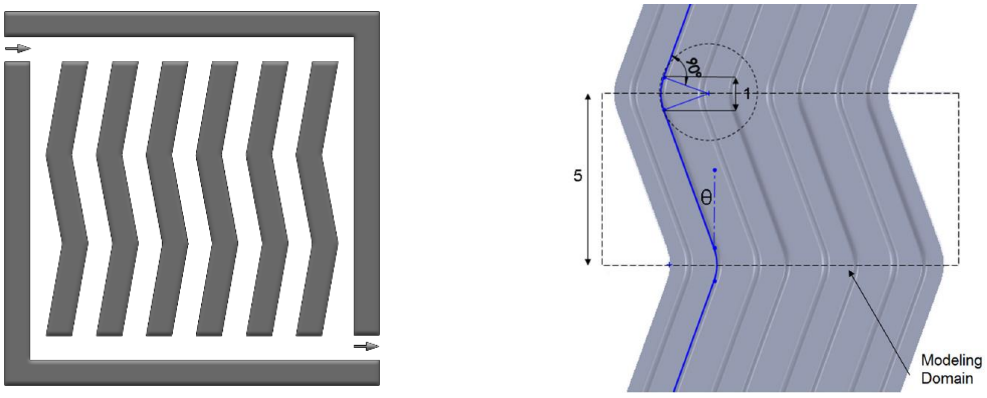

(a) (b)

Figure 2.3. Wavelike flow field: (a) Schematic diagram, (b) Previous study (Zhou and Chen, 2015).

Serpentine flow fields (see pattern in Figure 2.4) are the most used due to the large length of the path (A.Heinzzel et al. 2009). This flow field presents the best gas distribution compared with the straight parallel pattern and better performance for current density and temperature distribution (Peng et al., 2014).

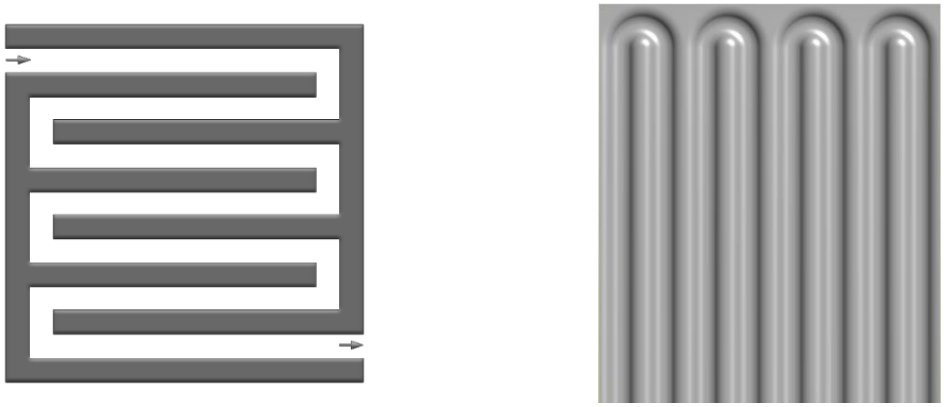

(a) (b)

Figure 2.4. Serpentine flow field: (a) Schematic diagram, (b) Simulation.

The basic serpentine flow field has the disadvantage of creating an excessive pressure drop from the two ends of the plate due to the extended length of the channel. This excessive pressure drop can originate a reactant gas short circuiting instead of the desired flow through the full length of the channel. One way to overcome this problem is to modify the design as illustrated in Figure 2.5, where the channels are subdivided into different segments. Each

segment has its own serpentine configuration with much shorter lengths. This solution results in an inferior pressure drop (Li and Sabir, 2005).

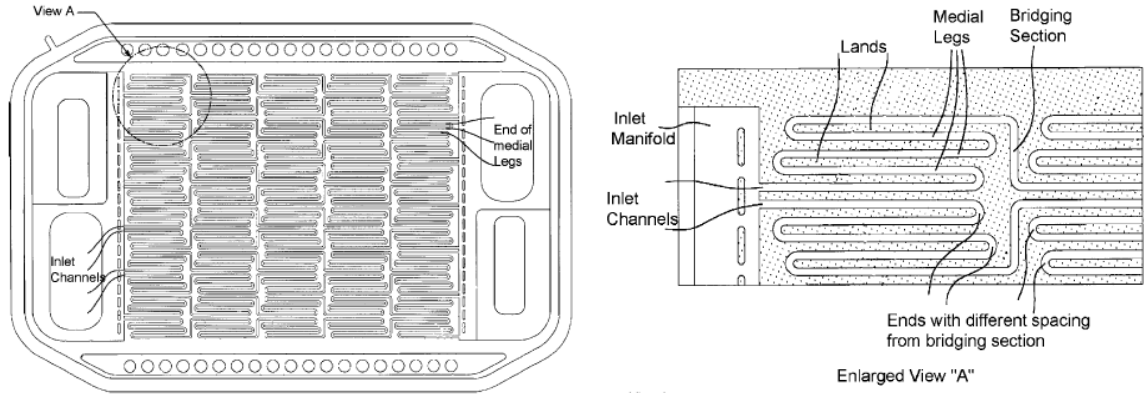

(a) (b)

Figure 2.5. Serially linked serpentine flow field (Li and Sabir, 2005).

Metallic bipolar plates use cooling flows on the opposite side of the plate, while the graphite plates use a separate cooling plate. Since the flow channels are produced by machining on graphite plates, distinct flow field configurations can be obtained for each side of the plate. However, metallic plates are typically manufactured by stamping processes, where the configuration of a flow field on one side of the plate determines directly the configuration on the opposite side. Therefore, it becomes difficult to obtain two continuous flow fields on both sides of the plate. For example, regarding the serpentine configuration presented in Figure 2.4 (a), the reactant flow is represented by the channel in white and the coolant flow is represented by the dark colour. Accordingly, the dark flow field is not continuous, as highlighted in Figure 2.4 (a). This problem can be solved using interdigitated flow plates as shown in Figure 2.6. In this case the reactant gas flow field is not continuous (see Figure 2.6.), hence the fluid is forced to flow through adjacent layers. Adapting this strategy on stamped metallic plates, the dark channel in Figure 2.6. (a) is continuous which improves the cooling flow.

The interdigitated flow field has been shown to improve fuel cells efficiency, however, only at the cost of a high pressure drop (Hu et al., 2009).

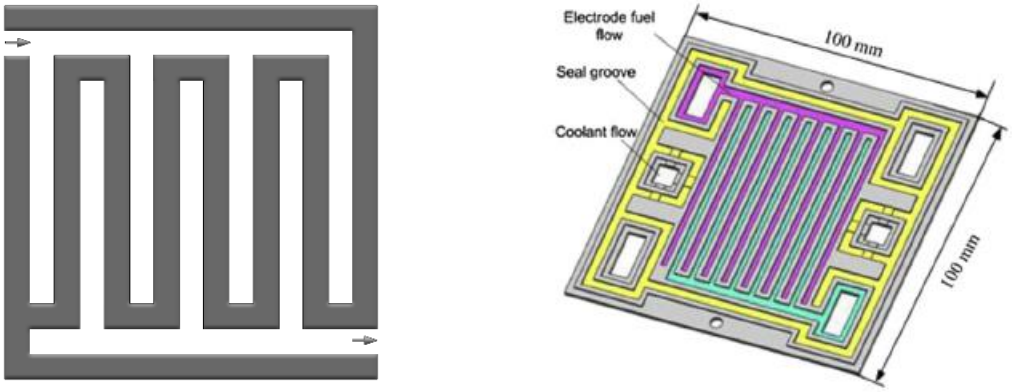

(a) (b)

Figure 2.6. Interdigitated flow field: (a) Schematic diagram, (b) CAD model (Peng et al., 2014).

2.2. Materials

The main material used for bipolar plates is graphite (Yoon et al., 2008). It offers good electrical conductivity, high corrosion resistance and low interfacial contact resistance. However, the cost of graphite plates is high due to their poor manufacturability and it has the disadvantage of being brittle and having poor permeability, which forces the use of thicker plates. In order to decrease the cost of fuel cells, metallic bipolar plates have received much attention lately, due to a much superior manufacturability, higher mechanical strength, being non permeable and more durable when submitted to shock and vibration, which is important when used for portable applications and transport (Peng et al., 2014).

The main handicap on metallic plates is the corrosion, which occurs in the acidic and humid environment present in a fuel cell. Some solutions for preventing metal degradation consist on using noble metals, stainless steels, aluminium alloys, titanium and nickel as a base metal and coating materials to prevent the corrosion on the base metal. Bipolar plates crafted with noble metals can achieve the performance of graphite plates or even higher but there is a large cost associated, which limits their commercialization. Cost wise, either the stainless steel or the aluminium plates are promising along with the correct coatings (Tawfik et al., 2007).

2.3. Forming Process

There are three main forming processes that can be applied in the manufacturing of metallic bipolar plates, namely:

- Microstamping;
- Hydroforming;
- Rubber pad forming.

The microstamping satisfies the requirements needed for bipolar plates manufacturing in terms of precision, production rate and cost effectiveness. In this process, expensive dies with adequate geometry are used to deform a thin sheet of metal as shown in Figure 2.7 (Peng et al., 2014).

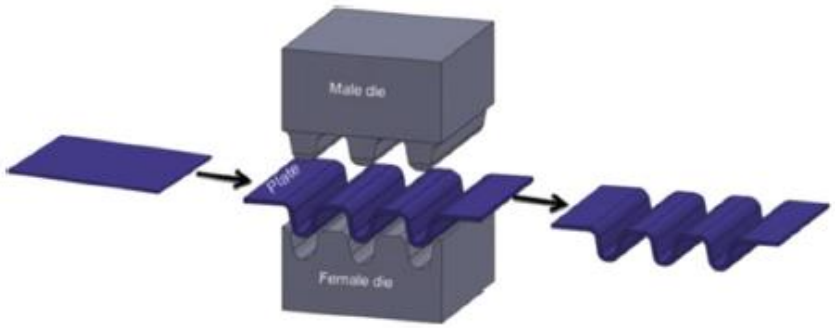

Figure 2.7. Representation of a microstamping process (Peng et al., 2014).

The hydroforming process is based on the application of a pressurized fluid which pushes the metal blank into a cavity with the desired shape. The schematic representation of this process is shown in Figure 2.8, where the fluid is represented in orange. This forming process allows to obtain higher drawing ratios, better surface quality and induces less springback in comparison with microstamping (Peng et al., 2014).

Figure 2.8. Representation of a hydroforming process.

Rubber pad forming is a process that has been growing in the automotive industry (Liu et al., 2010). It only requires the manufacture of one rigid die since the second one is replaced by a rubber pad as shown in Figure 2.9. This method, allows to improve the quality obtained and since only one die needs to be accurately manufactured, the cost and time can be greatly reduced. Furthermore, the tools assembly is not required to be precise. The adoption of a rubber pad as tool provides a contact force more distributed along the metal sheet, improving the formability (Liu et al., 2010).

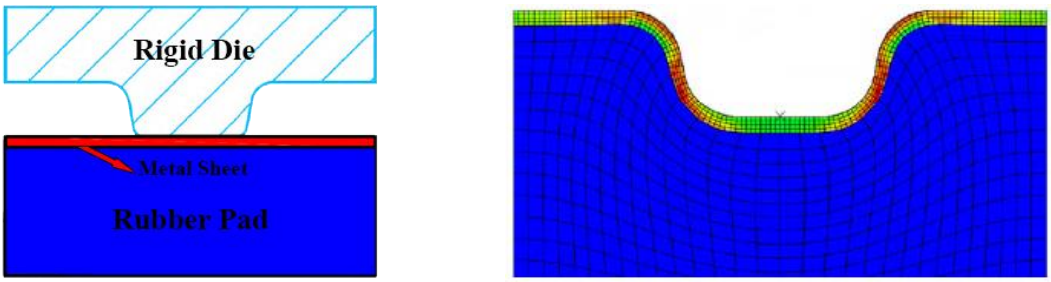

(a) (b)

Figure 2.9. Rubber pad forming: (a) Schematic diagram, (b) Simulation results (Liu et al., 2010).

The formability is influenced by the adopted sheet metal forming process, but the channel design should also be taken into consideration. In addition, the channel dimension design also has an important impact on the fuel cell performance since it influences the water and reactant transport as well as the reactant utilization efficiency (Peng et al., 2014).

Various parameters have influence on the stamping process such as the channel depth, *h*, the width of the channel, *w*, the width of the rib, *s*, the draft angle, α, the fillet radius, *R* of the tools and the blank thickness, *t* (Liu et al., 2010). The channel dimension design can be seen in Figure 2.10.

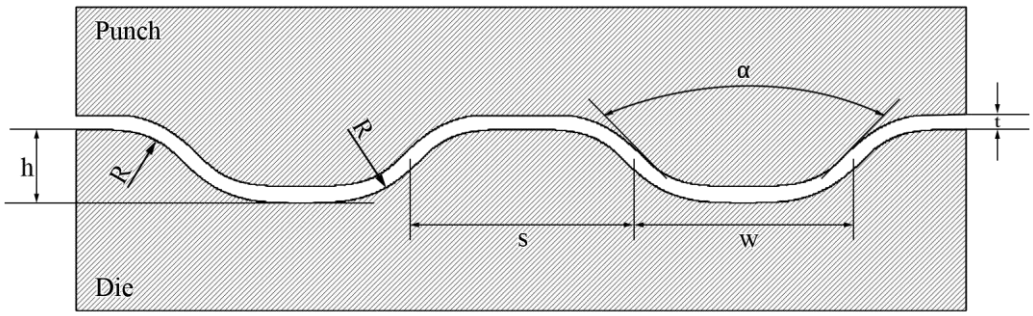

Figure 2.10. Representation of tools' dimensions.

The thickness of the blank used in the bipolar plates ranges between 0.051 mm and 0.3 mm depending on the blank's material, as shown in Table 2.2. Blanks with an initial thickness of 0.1 mm are widely used for stainless steel. In fact, using stainless steel, the thickness can be reduced to 0.1 mm and still maintain sufficient mechanical strength (Park et al., 2016). Aluminium bipolar plates with higher initial thickness were also studied by other authors.

Table 2.1. Summary on blank thickness used for metallic bipolar plates.

Blank Initial Thickness, t (mm)	Material	References
0.051	SS 304, SS 316	(Mahabunphachai et al., 2010)
0.1	SS 304, SS 316	(Liu and Hua, 2010) (Park et al., 2016) (Zhou and Chen, 2015) (Liu and Hua, 2010) (Liu et al., 2010) (Yi et al., 2015) (Peng et al., 2014)
0.2	SS 316	(Yi et al., 2015)
0.2	Al 1050	(Son et al., 2012)
0.3	Al 1050	(Son et al., 2012)

2.3.1. Influence of the main process parameters

The fillet radius, R, represented in the Figure 2.10, can influence the stamping results, improving the formability with its increase. Several authors include this parameter in their analysis for fuel cell efficiency (Peng et al., 2014). A summary on the fillet radius values used in metallic bipolar plates can be seen in Table 2.2. It ranges between 0.1 mm and 0.5 mm.

Table 2.2. Summary on fillet radiuses used for metallic bipolar plates.

Fillet Radius, R (mm)	Material	References
0.1	SS 304, SS 316	(Liu and Hua, 2010) (Park et al., 2016)
0.2	SS 304, SS 316	(Liu and Hua, 2010) (Mahabunphachai et al., 2010) (Zhou and Chen, 2015)
0.2	Al 1050	(Son et al., 2012)
0.25	SS 304, SS 316	(Mahabunphachai et al., 2010) (Zhou and Chen, 2015)
0.3	SS 304, SS 316	(Liu and Hua, 2010) (Zhou and Chen, 2015) (Liu et al., 2010)
0.5	SS 304, SS 316	(Peng et al., 2014)
0.5	Al 1050	(Son et al., 2012)

The draft angle, α (see Figure 2.10), also has an important role on the forming process. It has been concluded that, similarly to the fillet radius, its increase improves the formability of the plate (Peng et al., 2014). Geometries without the use of draft angles, i.e. zero draft angle (Hu et al., 2015) and draft angels up to 30° (Son et al., 2012) have been studied.

The dimensions used in order to obtain the best performance of a fuel cell for reaction efficiency are very different for the best dimensions to improve formability. A compromise has to be made in order to obtain the best efficiency and good formability. Results demonstrated that the highest efficiency, while maintaining good formability have been settled to 79% with a channel depth, h (see Figure 2.10), of 0.5 mm (Peng et al., 2014). It can also be seen different depths studied in Table 2.3. The channel depth ranges between 0.15 mm and 1.2 mm.

Table 2.3. Summary on channel depths used for metallic bipolar plates.

Channel Depth, h (mm)	Material	References
0.15	SS 304	(Peng et al., 2014)
0.26	SS 439	(Peng et al., 2014)
0.4	SS 304	(Peng et al., 2014)
0.4	Al 1050	(Son et al., 2012)
0.45	SS 304	(Peng et al., 2014)
0.5	SS 304	(Peng et al., 2014) (Zhou and Chen, 2015) (Liu and Hua, 2010)
0.55	SS 304	(Peng et al., 2014)
0.6	SS 304	(Peng et al., 2014) (Liu et al., 2010)
0.65	SS 304	(Peng et al., 2014)
0.75	SS 304, SS316	(Peng et al., 2014) (Mahabunphachai et al., 2010)
0.8	SS 304, SS316	(Park et al., 2016)
0.98	SS 304	(Peng et al., 2014)
1.2	SS 304	(Peng et al., 2014)

The rib width, s, and the channel width, w (see Figure 2.10), can influence the formability and the efficiency of the fuel cell. The values can vary from 0.15 mm to 2.0 mm (Peng et al., 2014). As previously described in section 1.2, the channel ensures the reactant flow through the bipolar plates and the rib manages the cooling fluid.

3. FINITE ELEMENT SIMULATION

The numerical simulations presented in this study were carried out with the in-house finite element code DD3IMP[1] (Menezes and Teodosiu, 2000), which was specifically developed for sheet metal forming simulation. Regarding its formulation, an updated Lagrangian scheme is used to describe the evolution of the deformation. In each increment, an explicit approach is used to obtain a trial solution for the nodal displacements and then Newton-Raphson algorithm is used to correct the first trial solution, which finishes when a satisfactory equilibrium state is achieved. This is repeated until the end of the process. The Newton-Raphson algorithm is used to solve both the non-linearities associated with the frictional contact and the elastoplastic behaviour of the deformable body, in a single iterative loop (Oliveira et al., 2007). In sheet metal forming processes, the boundary conditions are defined by the contact established between the metallic sheet and the forming tools. The friction contact is defined by Coulomb's classical law and the friction coefficient is set as 0.1 for the present work.

The forming tools are considered perfectly rigid in the numerical model, thus only their exterior surface are described in the numerical model. In this study the tool's surface is discretized with quadrilateral elements and is then smoothed with Nagata patches (Neto et al., 2014).

The discretization of the blank was carried out with isoparametric, 8-node hexahedral finite elements associated with a selective reduced integration (Menezes and Teodosiu, 2000) (Hughes, 1980).

[1] DD3IMP – Contraction of "Deep Drawing 3D IMPlicit finite element code" (Menezes and Teodosiu, 2000).

3.1. Materials

The material used for the stamping process of metallic bipolar plates has a large influence on the manufacturing process as discussed in section 2.2. Three different alloys for the blank were evaluated. Two sets of aluminium alloys (Al 5042 and Al 1235) and a stainless steel (SS 304) were chosen. The aluminium Al 5042 is already present in the DD3IMP materials database, hence its utilization. In the present study, two hardening laws are used, depending on the material selected. The Voce's hardening law (see equation (3.1)) is usually used to describe aluminium alloys since it has hardening behaviour with saturation. On the other hand, the Swift's hardening law (see equation (3.2)) is more adequate for mild steels. All the simulations performed in this study consider isotropy in the elastic and plastic behaviour (von Mises).

$$Y = Y_0 + (Y_{sat} - Y_0)[1 - \exp(-C_y \cdot \bar{\varepsilon}^p)] \tag{3.1}$$

$$Y = K(\varepsilon_0 - \bar{\varepsilon}^p)^n \tag{3.2}$$

Figure 3.1 shows the stress-strain curves for different metals, the choice of aluminium and stainless steel for stamped metallic plates becomes evident since the elongation before necking occurs at larger plastic strain values than for other materials.

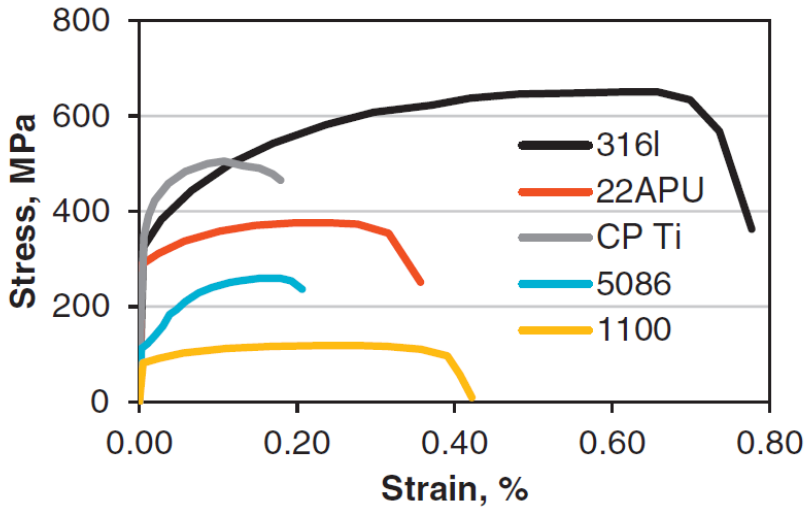

Figure 3.1. Stress-strain behaviour for different metals (Smith et al., 2014). Note: error on the units for the strain.

The Al 5042 aluminium alloy is described by the Voce hardening law (see equation (3.1)). The constitutive parameters for this aluminium alloy considering a blank thickness of 0.2083 mm can be seen in Table 3.1 (Neto et al., 2015).

Table 3.1. Voce's hardening law parameters and elastic properties for Al 5042 with a blank's initial thickness of 0.2083 mm.

	E (GPa)	v	Y_0 (MPa)	Y_{sat} (MPa)	C_y
Al 5042	68.9	0.33	267.80	375.08	17.859

The aluminium alloy Al 1235 (Hadi, 2014) and the stainless steel SS 304 (Liu et al., 2010) are described by Swift's hardening law (See equation (3.2)) since previous studies already implemented these materials with Swift's hardening law despite of Voce's hardening law being more appropriate for aluminium.

Liu et al., (2010) described the Swift's hardening law in function of the blank's initial thickness, *t*, as presented in equation (3.3). The equation has been converted from ksi to MPa.

$$Y = (1751.959t^2 - 677.479t + 319.848)\varepsilon^{(-1.703t^2 + 0.578t + 0.249)} \text{ [MPa]} \quad (3.3)$$

The aluminium alloy Al 1235 and the stainless steel SS 304 use hardening laws described from previous studies, due the time consumption and costs associated with experimental tensile tests. The constitutive parameters for a blank thickness of 0.1 mm for aluminium Al 1235 and stainless steel SS 304 can be seen in Table 3.2.

Table 3.2. Swift's hardening law parameters and elastic properties for Al 1235 (Hadi, 2014) and SS 304 (Liu et al., 2010) with a blank's initial thickness of 0.1 mm.

	E (GPa)	v	Y_0 (MPa)	K (MPa)	n
Al 1235	80	0.30	32.93	270.66	0.293
SS 304	162.5	0.30	192.2	850.68	0.206

Swift's hardening law can describe the aluminium behaviour but some aspects have to be taken into account when applying it for stainless steel. When stainless steel reaches the plastic deformation domain, microstructural changes trigger changes of mechanical

properties. A phase transformation from austenite to martensite can occur which induces simulation errors when applying Swift's hardening law. Studies found that while maintaining low strain rates, the volume fraction of martensite is decreased (Msolli et al., 2016).

Simulations applying Swift's hardening law to stainless steel in this study are acceptable if the simulations represent low strain rates in the stamping process of the metallic bipolar plates. The stress-strain curve for the three materials in use in this study can be seen on Figure 3.2.

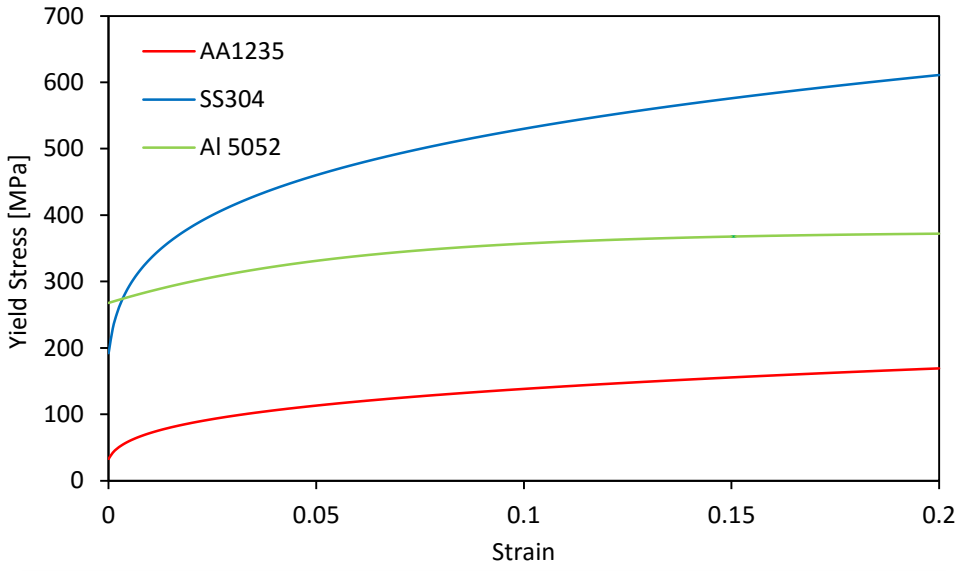

Figure 3.2. Stress-strain behaviour of the metals studied.

3.2. Boundary Conditions

The proper use of boundary conditions is fundamental to get accurate results in the numerical simulations. In fact, a body unrestrained with applied load presents infinite displacements. In this study, the boundary conditions were set to represent as close as possible the stamping process. Besides, in order to avoid excessive computational costs, only specific zones of the bipolar plate were analysed. Accordingly, the boundary conditions had to be adapted in order to represent the correct conditions of the selected representative zones looking for symmetries, which allow a portion of the structure to be analysed.

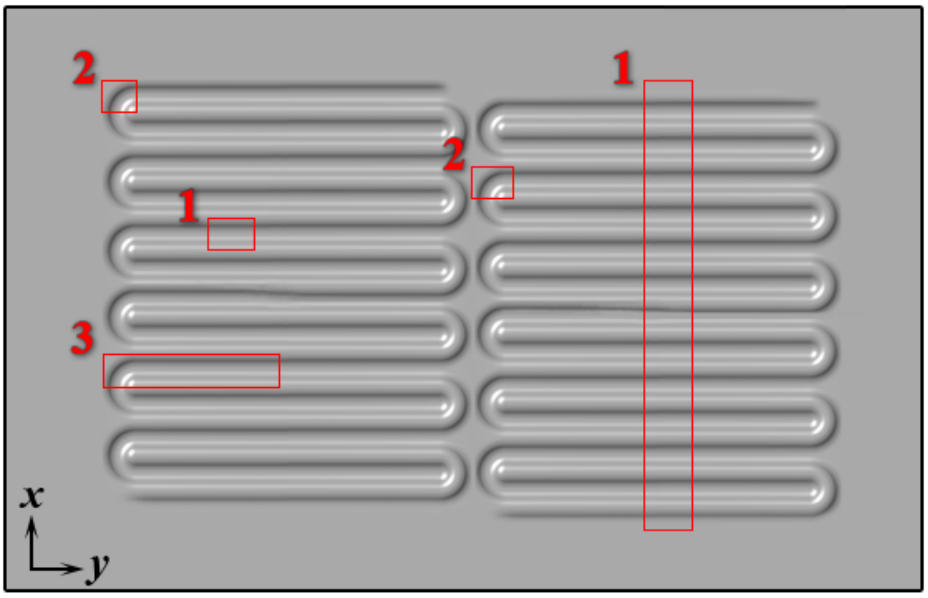

Figure 3.3. Representation of a serpentine flow field indicating the selected zones analysed.

Figure 3.3 indicates the different representative zones selected in this study for a serpentine flow field. Each representative zone aims to study a different region of the bipolar plate, covering the entire deformation behaviour found in the plate.

1. The first representative zone represents half channel (see Figure 3.4). Adequate boundary conditions are required to represent the symmetry of the channel. Thus, the red plane and its parallel plane on the other extremity represent the constrain in the *x* direction. In the same way, the blue plane and its parallel plane on the other extremity represent the constrain in the *y* direction (plane strain deformation). These conditions were chosen since channels display symmetric geometry and load. These boundary conditions represent the most unfavourable conditions for the forming process, since they constrain the material flow into the cavity. Besides the study on half channel, ten channels will be studied to verify the influence of excess material at both extremities.

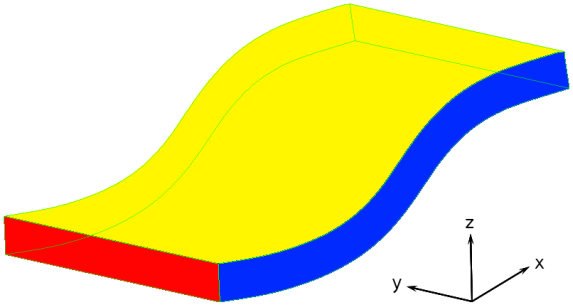

Figure 3.4. Representation of the boundary conditions for section 1.

2. The curved representative zone must also be studied. In this case, the end of the plate does not represent any symmetry, then the boundary conditions on such extremities can be set free. Figure 3.5 presents the red plane which constrains the *x* direction and the blue plane constrains the *y* direction.

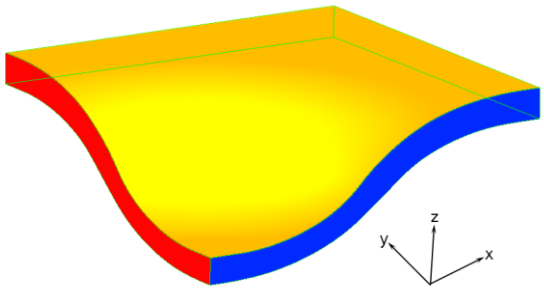

Figure 3.5. Representation of the boundary conditions for section 3.

This representative zone is favourable to the stamping process, a zone adjacent to other channels must be studied where material cannot flow as easily since adjacent channels are also being formed having here symmetry in load and geometry. This type of restriction is applied to field flows such as a serially linked serpentines (see Figure 2.5). The same simulation is performed but introducing boundary condition of symmetry on the four extremities.

3. This section is meant to study the influence of the straight channel on the curved section, since section 2 does not take this into account. Constraints are defined similarly to other sections, i.e. boundary conditions of symmetry on the four extremities.

3.3. Parametric Model

To create the tool's geometry a CAD program was used. Since the tools behave as rigid bodies, only the outer surface was created using CATIA® V5. In order to guarantee the symmetry of the final geometry, the dimensions were set on a mid-plane between the punch and the die (see Figure 3.6) while the tool's dimensions are obtained with an offset. The distance between the punch and the die were maintained equal to the blank's initial thickness. These dimensions were maintained as variables and exported to Excel in order to change the geometry for different configurations (see Appendix A).

Seven parameters for this study's final geometry were exported and varied (see Figure 3.6):

- Channel depth, *h*;
- Channel width, *w*;
- Rib width, *s*;
- Blank's initial thickness, *t*;
- Fillet radius, *R*;
- Main radius, *r*;
- Flat section, *a*.

Contrary to the classical geometry presented in Figure 2.10, the draft angle is not represented but it depends on the tool's radius applied, the larger the radius is, the larger the draft angle will be. An additional variable is added to the geometry, which is the fillet radius, *R*.

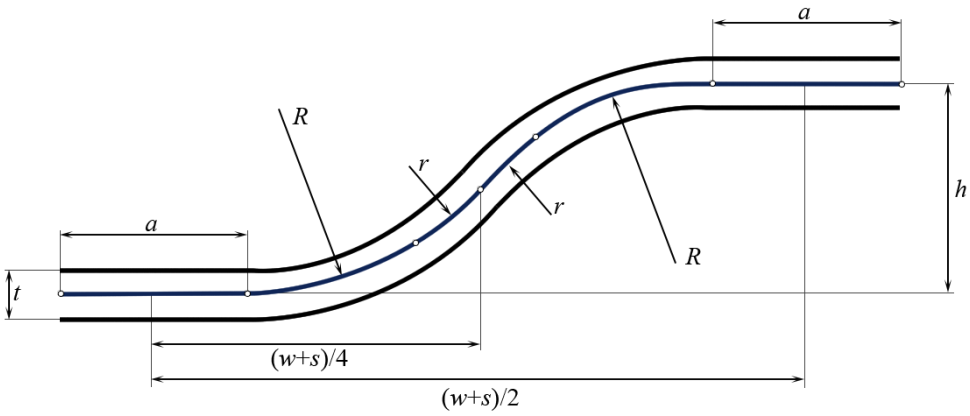

Figure 3.6. Parametric model for the final geometry of the tools.

From the model represented in Figure 3.6, an extruded surface was created for the straight channel. In order to represent the curved section of the simplified model (see Figure 3.3) only a revolved surface from the initial sketch was required, instead of the extruded surface. Both of the tools' models can be seen in Figure 3.7.

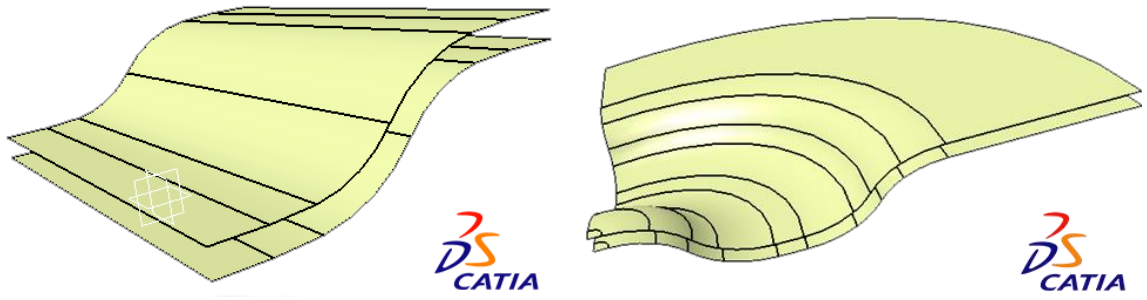

(a) (b)

Figure 3.7. Tools' geometry on CATIA® V5: (a) Straight channel, (b) Curved section.

With the tool's surface modelled, the next step consists in exporting the surface in IGES format for further meshing with the pre-processing program GID®. The first step is to verify the surface's normal orientation for simulation purposes. This orientation must be as indicated in Figure 3.8, i.e. surface normal vectors pointing towards the blank.

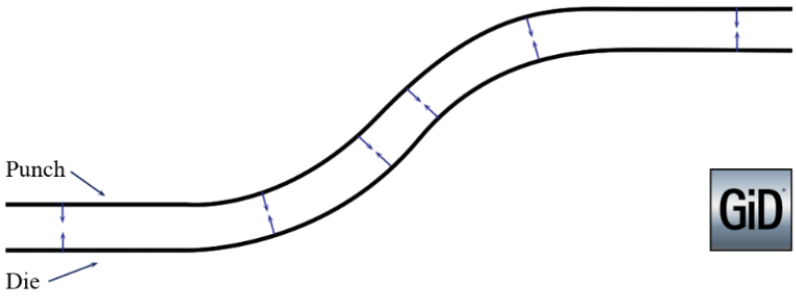

Figure 3.8. Orientation of the surfaces representing the tools geometry.

The discretization of the tool's surface will be carried in order to present always two finite elements along the width for the simulations of the straight channel. For the curved sections, nine elements along the radius are used (Neto, 2014). For every straight surface along the length, only one finite element is required. For the curved surfaces, two elements are required to be smoothed with Nagata patches' quadratic interpolation. The final mesh for the straight channel die, before being smoothed, is shown in Figure 3.9.

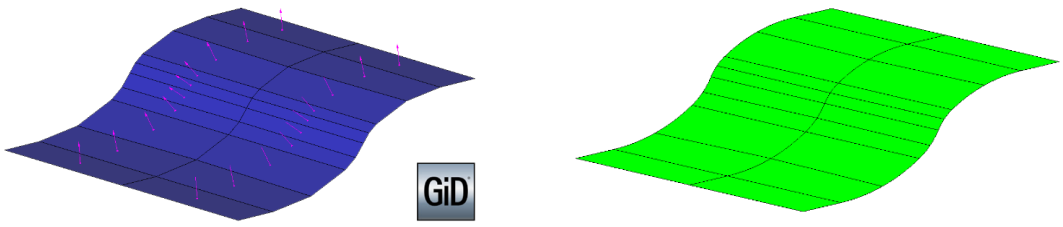

(a) (b)

Figure 3.9. Mesh representation for the die (a) Before being smoothed, (b) After being smoothed.

The maximum shape error can be obtained with equation (3.4), where y is the shape error in percentage and x is the normalized arc length (Neto et al., 2013).

$$y = 0.8864x^{4.0854} \ [\%] \tag{3.4}$$

The maximum error occurs on the tool's radius thus both radius used must be verified (see Figure 3.6). The normalized arc length for both radiuses can be obtained with the dimensions shown in Figure 3.10 and the equations (3.5) and (3.6).

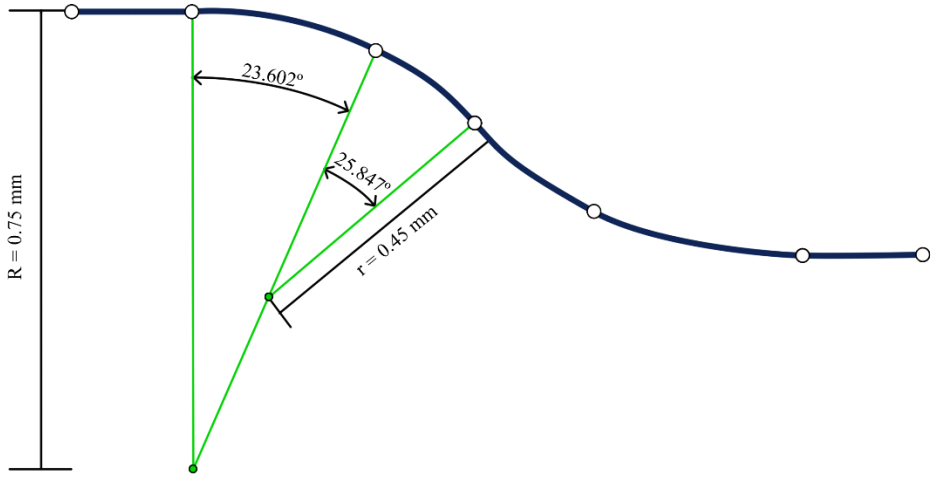

Figure 3.10. Die's geometry and dimension necessary to obtain the shape error.

$$x = \frac{l}{r} = \frac{\frac{\alpha\pi r}{180}}{r} = \frac{\alpha\pi}{180} = \frac{23.602\pi}{180} = 0.412 \tag{3.5}$$

$$x = \frac{l}{r} = \frac{\frac{\alpha\pi r}{180}}{r} = \frac{\alpha\pi}{180} = \frac{25.847\pi}{180} = 0.451 \tag{3.6}$$

With equation (3.4), the shape error for the fillet radius is 0.024% (see equation (3.7)) and the shape error for the main radius is 0.034% (see equation (3.8)). The shape error as close to non-influence on the results obtained for this study.

$$y = 0.8864x^{4.0854} = 0.8864 \cdot 0.412^{4.0854} = 0.024\% \tag{3.7}$$

$$y = 0.8864x^{4.0854} = 0.8864 \cdot 0.451^{4.0854} = 0.034\% \tag{3.8}$$

The tools can then be exported to the finite element code DD3IMP for further simulation. The mesh of the blank is generated on the finite element program using a single finite element along the width for 2D simulations (plane strain deformation) representing half a channel. For the length of the blank the number of elements will vary, to be able to maintain the quadratic elements as square as possible, as shown in Figure 3.11 (a). For

simulations which represent the curved sections, the number of elements along the width of the blank will also vary to maintain cubic elements as shown in Figure 3.11 (b).

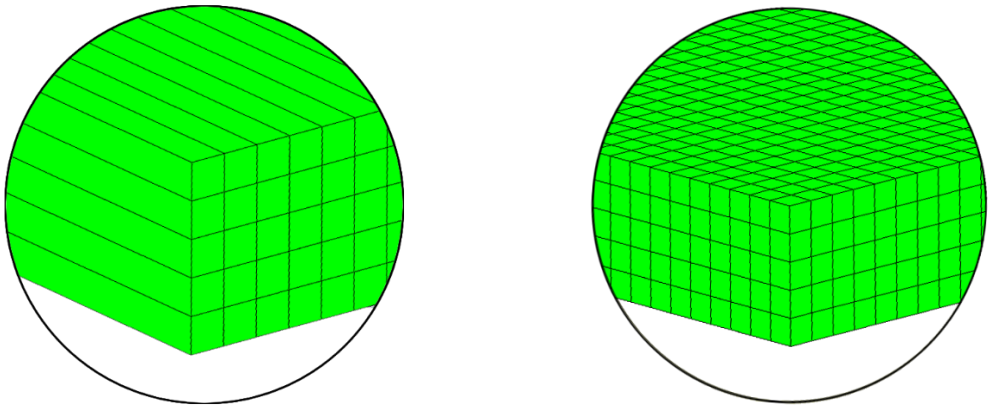

(a) (b)

Figure 3.11. Finite element mesh generation in detail: (a) 2D simulation, (b) 3D simulation.

After the process of creating a parametric model and the finite element mesh, simulations are ready to proceed. The computer used has the following characteristics:

Processor:	Intel®Core™ i7-2600K CPU @ 3.40 GHz
Installed memory (RAM):	8.00 GB
System Type:	64-bit Operating System

3.4. Microstamping

A microstamping process as shown in Figure 2.7 is replicated for this study. The process is divided in two phases: first the die is maintained stationary while the punch moves towards the blank to form the desired shape. This phase ends when the distance between both tools is equal to the blank's initial thickness. The second and final phase is the removal of both tools in a single instant for the springback effect to occur.

Both plastic strain and thickness reduction are studied as principal parameters to evaluate the formability of the channel.

3.4.1. Influence of the finite element size

The finite element size is important to verify the error committed during the simulation. Since the objective is to maintain at all times the square form of the finite element, only the number of elements along the blank's thickness (and subsequently its size) were studied. The finite element size along the blank's length varied to maintain the desired form and the one element along the width was not altered.

The number of finite elements along the blank's thickness has been changed between two and nine, corresponding to an element size between 0.011 and 0.05 mm. In each case the error was obtained in function of the simulation with the highest number of finite elements comparing the value obtained for the maximum thickness reduction. The result was an error inferior to 0.01% which is highly acceptable. Figure 3.12 shows the thickness reduction of the blank for each simulation. For the minimum thickness all simulations represent the correct value with a small error. Adopting four finite elements along the thickness, a good overall results can be obtained as shown in Figure 3.12.

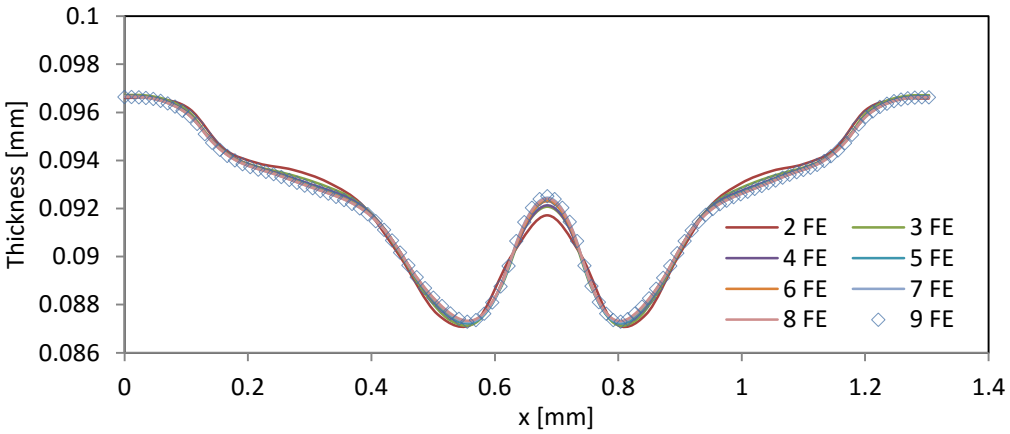

Figure 3.12. Final thickness distribution in function of the number of finite elements along the blank's thickness.

The number of finite elements has a smaller influence on the punch force than on the thickness reduction as shown in Figure 3.13. Four or more finite elements reduce or completely remove the incorrect behaviour in the punch force. Hence, in this study the use of four elements along the thickness for the finite element simulations. Increasing the number of finite elements reduces the simulation error but at the cost of an increase in processing time. Besides, using an even number of finite elements along the thickness allows to use the mid-plane as a reference for thickness measurements.

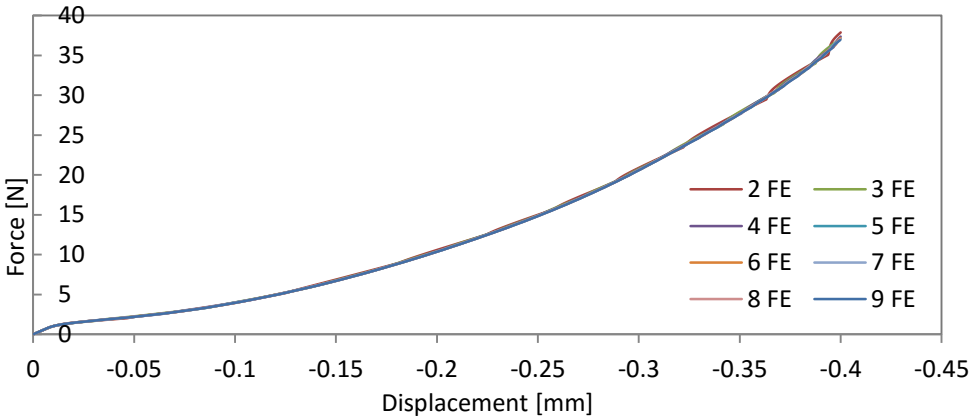

Figure 3.13. Punch force evolution in function of the number of elements along the blank's thickness.

3.4.2. Influence of the boundary conditions

Two simulations were performed to verify the influence of the boundary conditions. The second simplified model in Figure 3.3 with ten channels is used. The first simulation recreates the conditions described in section 3.2 while the second simulation only applies a boundary condition for the middle value of *x* without restrictions on the extremities along the *x* direction.

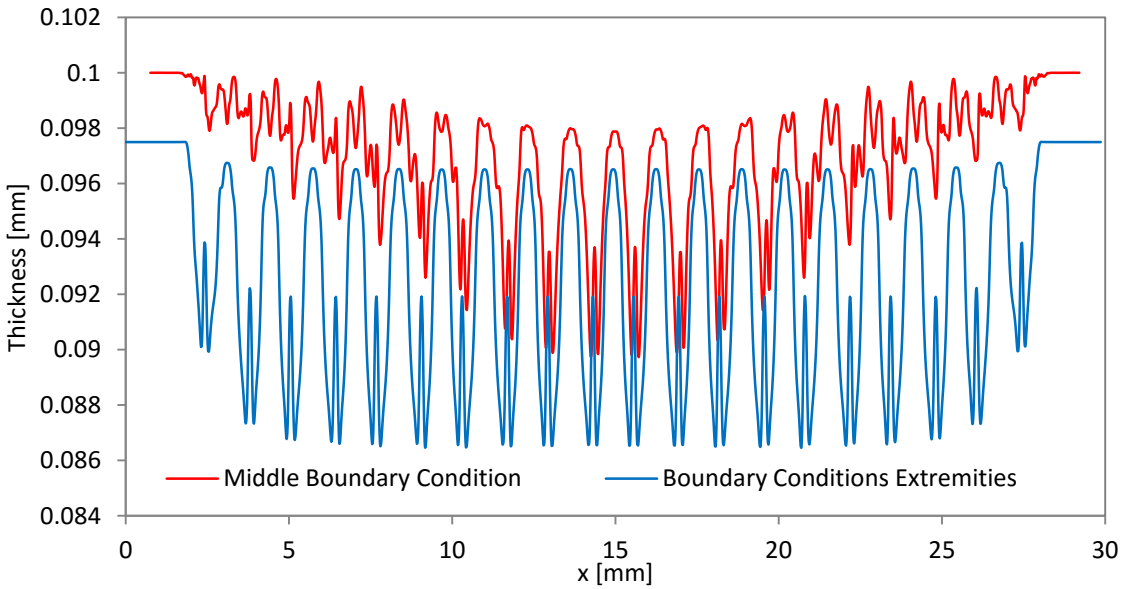

Figure 3.14. Final thickness distribution for simulations with different boundary conditions and a ten channel simplified model.

The simulation with the boundary conditions on the extremities has an increased thickness reduction compared with the simulation with the boundary condition in the middle. Besides, the model using free extremities provides a more uniform thickness distribution as shown in Figure 3.14. For this study, the most disadvantageous model will be used with the boundary conditions on the extremities since any other model can achieve better results. Additionally, the final thickness distribution is more uniform, allowing an easier contact between each flow channel and the membrane with an inferior dimensional error.

3.4.3. Primary optimization

The first simulation presents a tool's geometry from Son et al. (2012) with the 5042 aluminium alloy for the blank (see section 3.1) considering half a straight channel. The tool's geometry follows the scheme shown in Figure 2.10 and the dimensions are indicated in Table 3.3.

Table 3.3. Tool's geometrical dimensions for Al 5042 (Son et al., 2012).

w [mm]	s [mm]	h [mm]	R [mm]	α [º]
1.2	0.4	0.4	0.4	30

The plastic strain distribution after forming is shown on Figure 3.15 for half a straight channel. The maximum value of plastic strain is about 0.6 and the thickness reduction is over 28%.

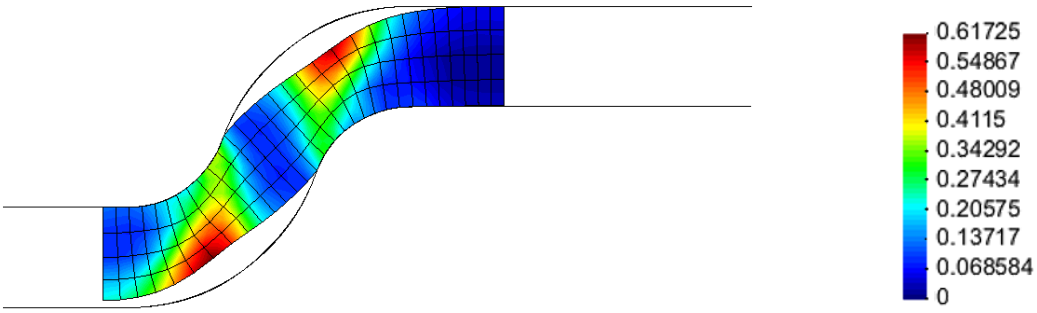

Figure 3.15. Plastic strain distribution for the geometry from Son et al. (2012) for a thickness of 0.2 mm (Al 5042).

Since 0.2 mm thickness is half of the channel depth, an attempt to reduce the thickness to 0.1 mm is made for the next simulation, taking in account the error which can occur since the aluminium parameters are described for a thickness of 0.2 mm.

The maximum value of plastic strain is around 0.83, as shown in Figure 3.16, presenting a thickness reduction of over 52%. Therefore, the reduction of the blank thickness induces an increase in the plastic deformation and occurrence of necking.

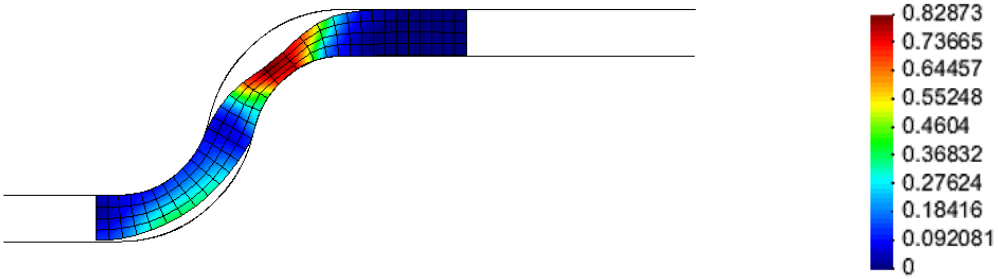

Figure 3.16. Plastic strain for the geometry from Son et al. (2012) for a thickness of 0.1 mm (Al 5042).

The evolution of the punch force for both thicknesses is presented in Figure 3.17. As expected, the force necessary to form the 0.2 mm blank is higher than the 0.1 mm blank. The sudden force increase at the end is due to a contact between the blank's extremity and the tool in the final steps. This contact force is displayed on the top right corner of Figure 3.18 (b). This force peak is common in this process due to the bending effect at the end of forming stage.

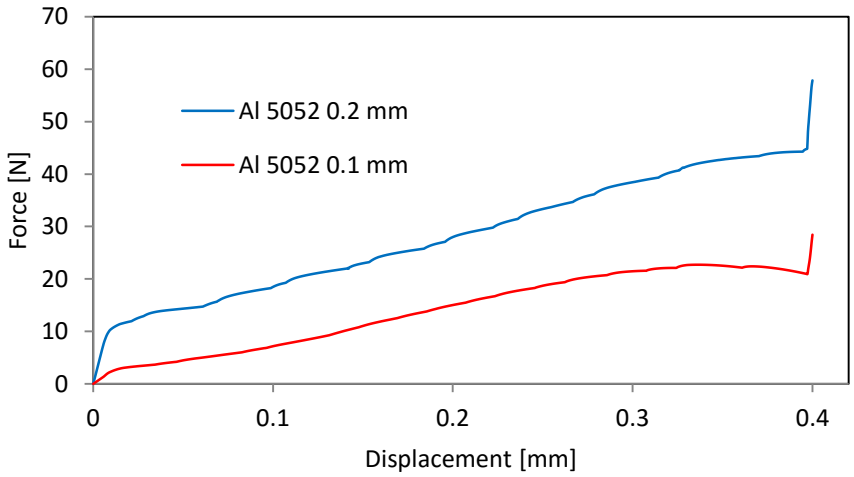

Figure 3.17. Punch force evolution for a thickness of 0.1 mm and 0.2 mm (Al 5042), considering the geometry from Son et al. (2012).

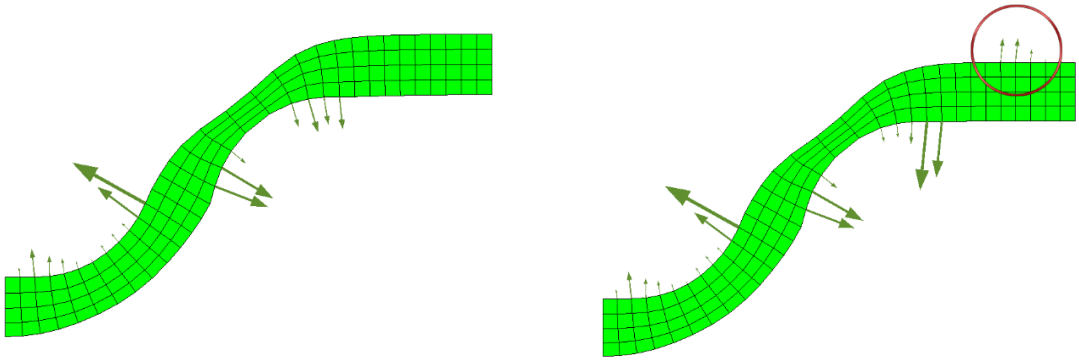

(a) (b)

Figure 3.18. Contact forces (a) Before the final contact, (b) During the final contact.

The results show a low formability for the 5042 aluminium alloy, as expected after the information obtained from Figure 3.1 regarding the 5XXX aluminium alloys. In order to improve the formability in the process, the 304 stainless steel will be used for forward simulations. Since stainless steel blanks with 0.1 mm thickness maintain sufficient mechanical strength (see section 2.3), this will be the thickness used for this study.

Maintaining the tool's geometry of previous simulations and with the use of 304 stainless steel, the maximum thickness reduction is over 35% with a maximum plastic strain of 0.6, as shown in Figure 3.19. These numerical results demonstrate that the adoption of 304 stainless steel allows to improve the thickness reduction for the same initial thickness and geometry.

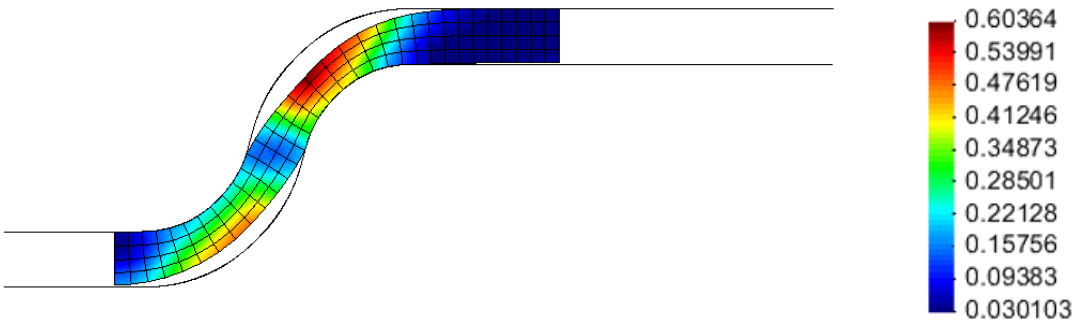

Figure 3.19. Plastic strain distribution for the geometry from Son et al. (2012) for a thickness of 0.1 mm (SS 304).

The punch force necessary to form the stainless steel is higher than the force required for the 5042 aluminium, as shown on Figure 3.20. This result is coherent with the stress-strain curve observed on Figure 3.2.

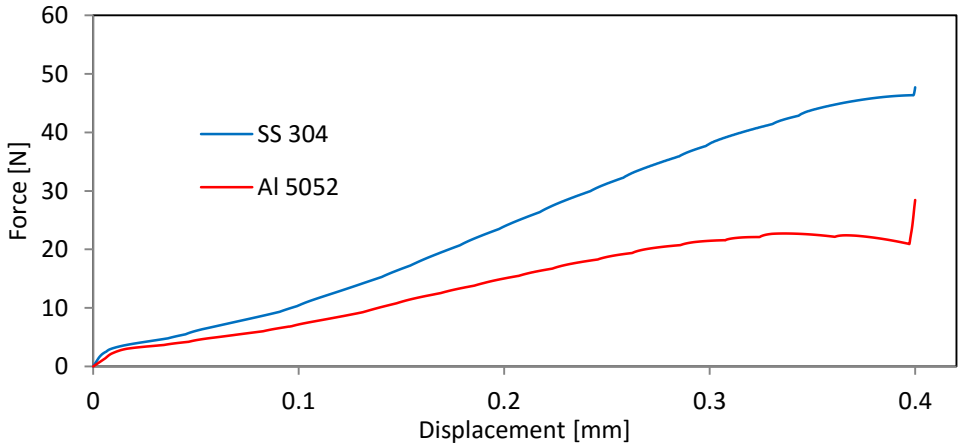

Figure 3.20. Punch force evolution for two different materials (Al 5042 and SS 304) considering the geometry from Son et al. (2012).

The numerical results demonstrate a critical thickness reduction in the channel, which jeopardise the fuel cell's mechanical strength. This is mainly due to the boundary conditions use in the finite element model. In order to increase the amount of material available to flow into the cavity, an increase in *s* and *w* dimensions (see Figure 2.10) was applied, maintaining the remaining dimensions unaltered. The obtained plastic strain distribution is presented in Figure 3.31.

The maximum value of plastic strain decreased to 0.45, while the thickness reduction is under 25%. The extra material available allows to improve material flow and, consequently, the formability of the blank.

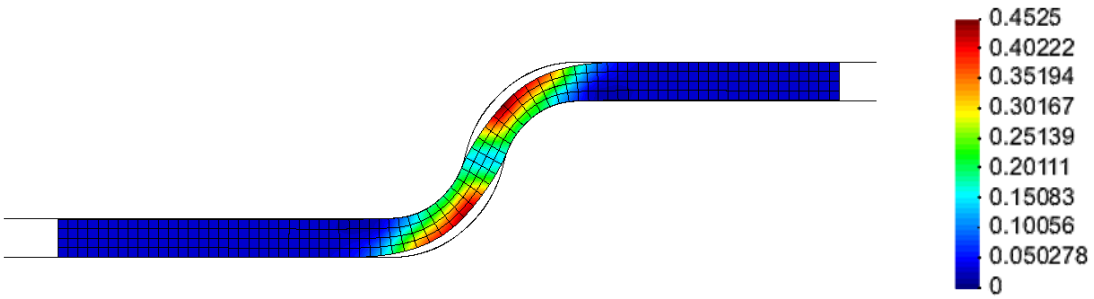

Figure 3.21. Plastic strain distribution for an increase in channel and rib width considering a thickness of 0.1 mm (SS 304).

In order to better understand the influence of the extended dimensions *s* and *w*, only the curved section of the 2D model is studied without the straight section of the channel. According to the results presented in Figure 3.22, the maximum value of plastic strain increased to 0.68, while the maximum thickness reduction is around 50%. The reduction in the formability was expected and the numerical results shown the near zero plastic strain on the highlighted area shown in Figure 3.22.

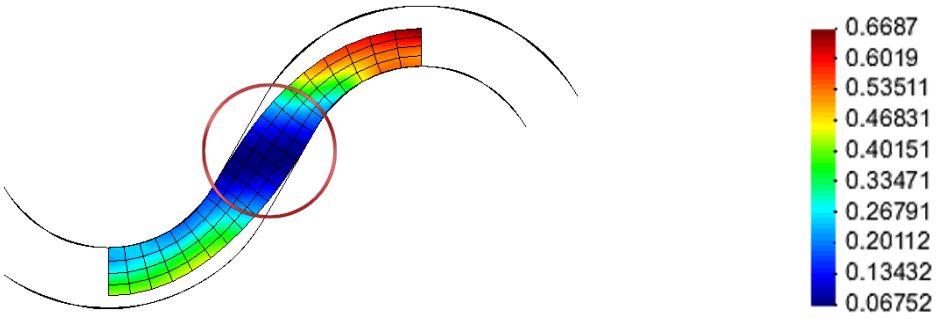

Figure 3.22. Plastic strain distribution for a geometry without a straight section for a thickness of 0.1 mm (SS 304).

In order to reduce the plastic strain in the critical areas (mainly on the 0.5 mm radius) of the stamped plate, the geometry of the forming tools was changed by means of the inclusion of a fillet radius, *R*, to distribute the plastic strain evenly along the plate (see Figure 3.6). The objective is to increase the plastic strain on the highlighted area shown in Figure 3.22, in order to decrease the plastic strain on the remaining critical areas. The dimensions of the model represented in Figure 3.6 are shown in Table 3.4.

Table 3.4. Tool's geometrical dimensions for an optimized geometry (SS 304).

***w* [mm]**	***s* [mm]**	***h* [mm]**	***R* [mm]**	***r* [mm]**	***a* [mm]**	***t* [mm]**
1.3	1.3	0.4	1.3	0.6	0.2	0.1

Figure 3.23 shows both the distribution of the thickness reduction and the plastic strain distribution. The maximum value of thickness reduction is only 12% and the maximum plastic strain is approximately 0.21. Thus. the methodology adopted has induced an overall improvement in formability of 65%.

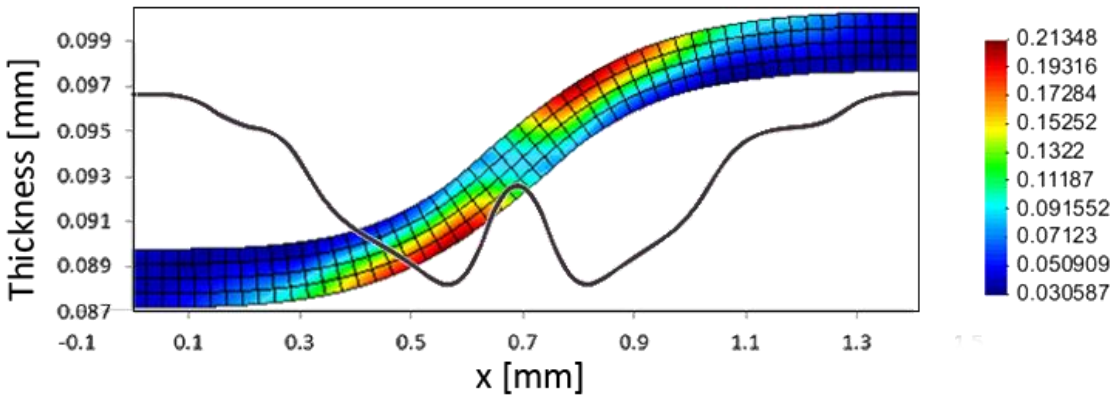

Figure 3.23. Plastic strain and thickness reduction for the new geometry for a thickness of 0.1 mm (SS 304).

The punch force evolution is shown on Figure 3.24. The maximum punch force presented is inferior to previous numerical results for the same material (see Figure 3.20).

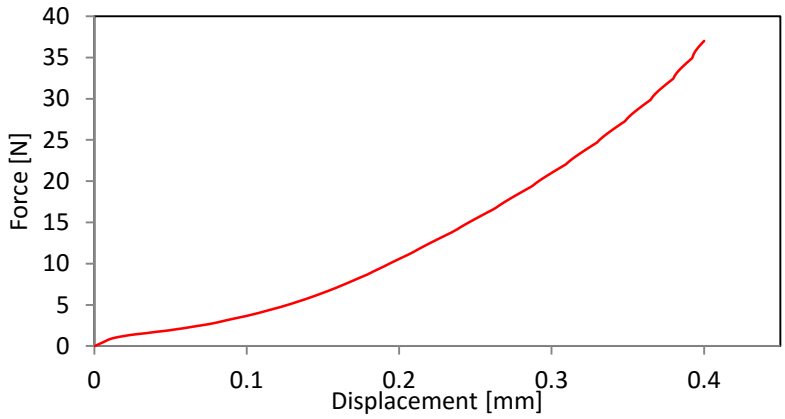

Figure 3.24. Punch force evolution for the new geometry for a thickness of 0.1 mm (SS 304).

A representation of a PEMFC with the new geometry of the bipolar plates is shown in Figure 3.25.

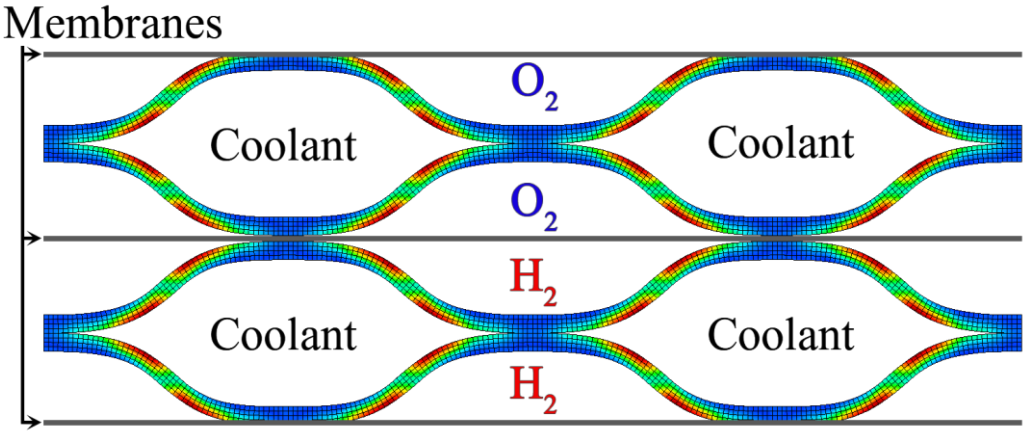

Figure 3.25. Representation of a PEMFC with the new geometry.

The chemical efficiency of the fuel cells is a key factor that should be taken into account in its manufacturing process. In section 2.3.1, a compromise between fuel cell efficiency and formability was discussed, the next tool geometry tries to replicate the geometry imposed for an efficiency of 79%, being the tool's dimensions shown in Table 3.5. Although the geometry tested for the best efficiency did not include the fillet radius, *R*, involved in the present model, the 1.3 mm radius has been used for the study and a plane section, *a*, of 0.20 mm was imposed. The plastic strain distribution presented in Figure 3.26 shows a maximum value of 0.31 and a maximum thickness reduction of 19%. Thus, for the new geometry of the tools, a greater reaction efficiency could be obtained than 79% maintaining an adequate mechanical strength.

Table 3.5. Tool's geometrical dimensions for a chemical efficiency of 79% (SS 304).

***w* [mm]**	***s* [mm]**	***h* [mm]**	***R* [mm]**	***r* [mm]**	***a* [mm]**	***t* [mm]**
1.0	1.6	0.5	1.3	0.5	0.2	0.1

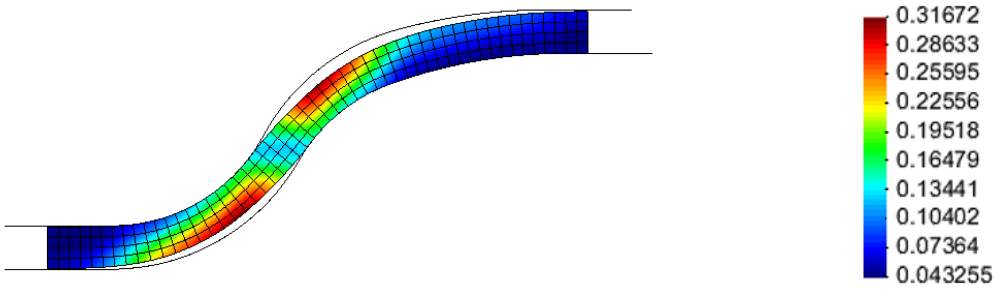

Figure 3.26. Plastic strain distribution for the bipolar plate geometry with 79% efficiency for a thickness of 0.1 mm (SS 304).

3.4.4. Influence of tool geometry parameters

A further improvement on the tool's geometry is required to obtain more favourable results regarding the formability of the blank. The main geometry parameters are:

- Channel depth, *h*;
- Fillet radius, *R*;
- Main radius, *r*;
- Channel and rib width, *w* and *s*;
- Flat section, *a*;
- Blank's initial thickness, *t*.

For a correct study on the influence of each parameter, the model created was symmetric, maintaining *s* and *w* identic and when analysed they are equally changed.

3.4.4.1. Channel depth, *h*

To evaluate the influence of the channel depth on the formability, the remaining parameters are unchanged and shown in Table 3.6.

The channel depth starts with a value equal to 0.3 mm and with an increment of 0.05 mm, for each simulation, until the thickness reduction reaches over 30%. In this case, the range is between 0.3 mm and 0.65 mm and the geometry of the die for these values is shown in Figure 3.27.

Table 3.6. Tool's geometrical dimensions for the study on the channel depth (SS 304).

w [mm]	*s* [mm]	*h* [mm]	*R* [mm]	*r* [mm]	*a* [mm]	*t* [mm]
1.2	1.2	0.3 – 0.65	1.3	0.5	0.2	0.1

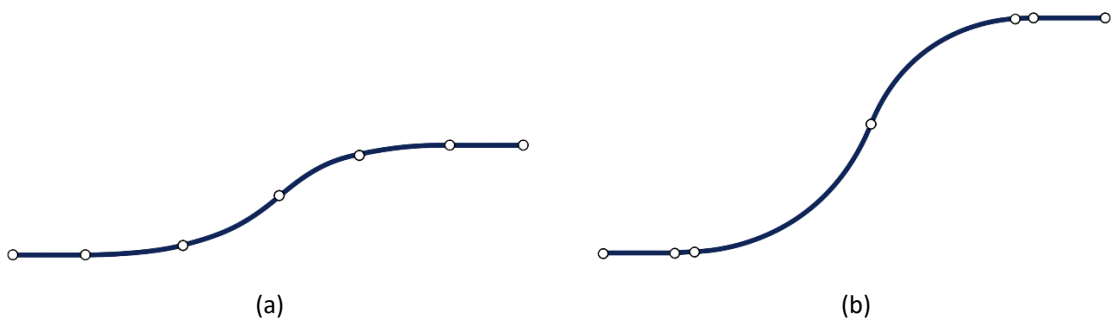

(a) (b)

Figure 3.27. Die geometry (a) Channel depth of 0.3 mm, (b) Channel depth of 0.65 mm.

Figure 3.28 shows the maximum thickness reduction obtained for different channel depths until the 30% thickness reduction is obtained. The maximum value of thickness reduction increases quadratically with the channel depth.

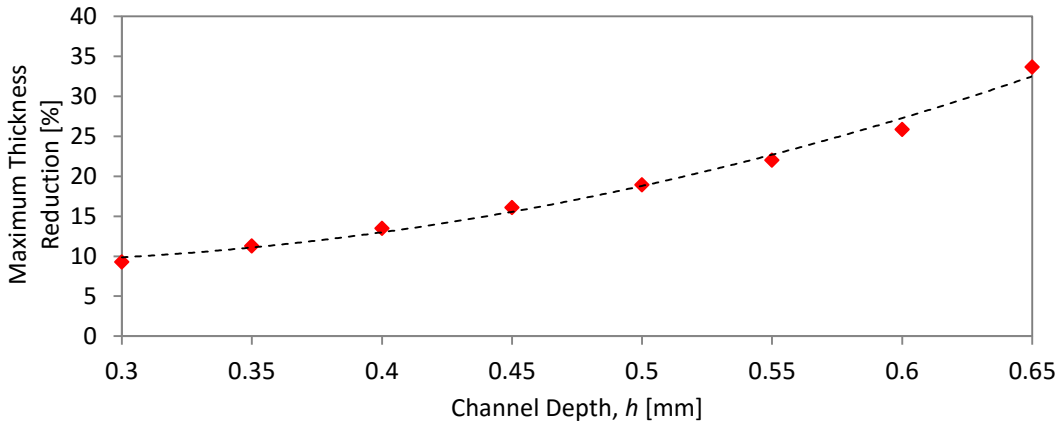

Figure 3.28. Maximum thickness reduction in function of the channel depth.

The evolution of the final thickness along the blank in shown in Figure 3.29 (a). The minimum value of the thickness occurs in the channel radius, presenting a symmetry, namely for small values of channel depth. The punch force increases as the channel depth increases as shown in Figure 3.29 (b). Until approximately 0.15 mm of punch displacement, the force evolution is coincident for all geometries analysed.

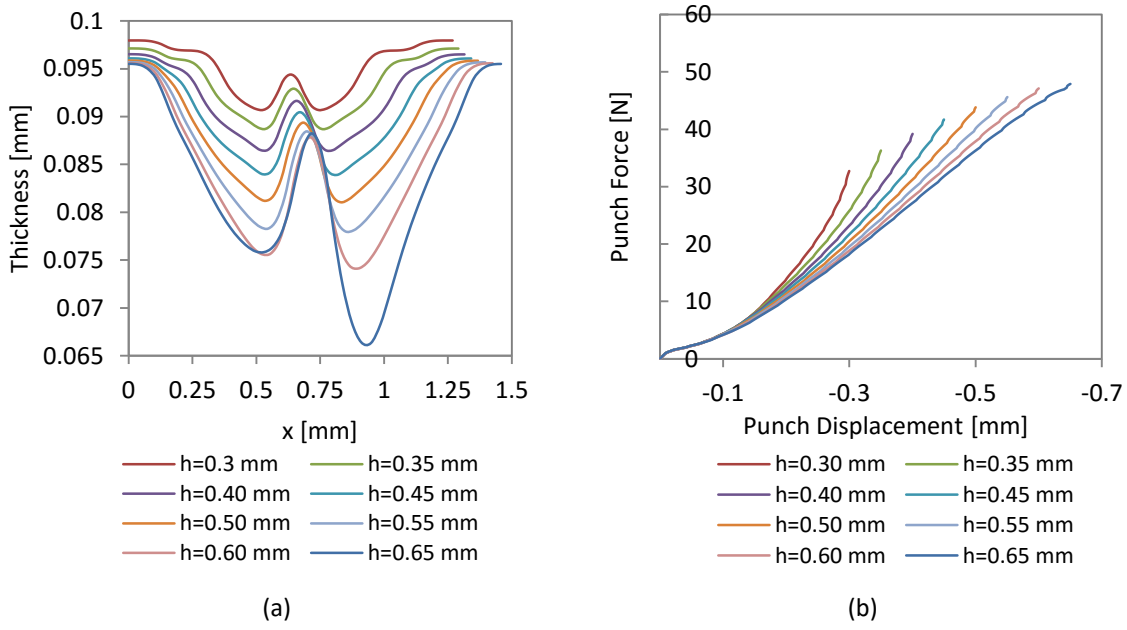

Figure 3.29. Influence of channel depth on: (a) Final thickness, (b) Punch force evolution.

3.4.4.2. Fillet radius, *R* and *r*.

In order to evaluate the influence of the fillet radius on the formability, the remaining parameters are set as shown in Table 3.7. The fillet radius starts with 0.8 mm due to the geometry constraints, using an increment of 0.1 mm for each geometry until the evolution on the formability stabilises. In this case, the range is between 0.8 mm and 1.5 mm which corresponds to the geometry of the die shown in Figure 3.30 (a) and (b), respectively.

Table 3.7. Tool's geometrical dimensions for the study on the a fillet radius (SS 304).

w [mm]	*s* [mm]	*h* [mm]	*R* [mm]	*r* [mm]	*a* [mm]	*t* [mm]
1.2	1.2	0.4	0.8 – 1.5	0.5	0.2	0.1

(a) (b)

Figure 3.30. Die geometry: (a) Fillet radius of 0.8 mm, (b) Fillet radius of 1.5 mm.

Figure 3.31 (a) presents the maximum value of thickness reduction obtained for different values of fillet radius. The value increases with a quadratic tendency, as shown in Figure 3.31 (a). The geometry presented in Figure 3.30 (b) shows the similarity with the first simulations obtained since the fillet radius tends to work as a flat section, providing results similar to the first simulations without the fillet radius. This observation also explains the reduction in formability. The impact of the fillet radius on the thickness distribution is insignificant as highlighted in Figure 3.31 (b), except for the fillet radius of small value.

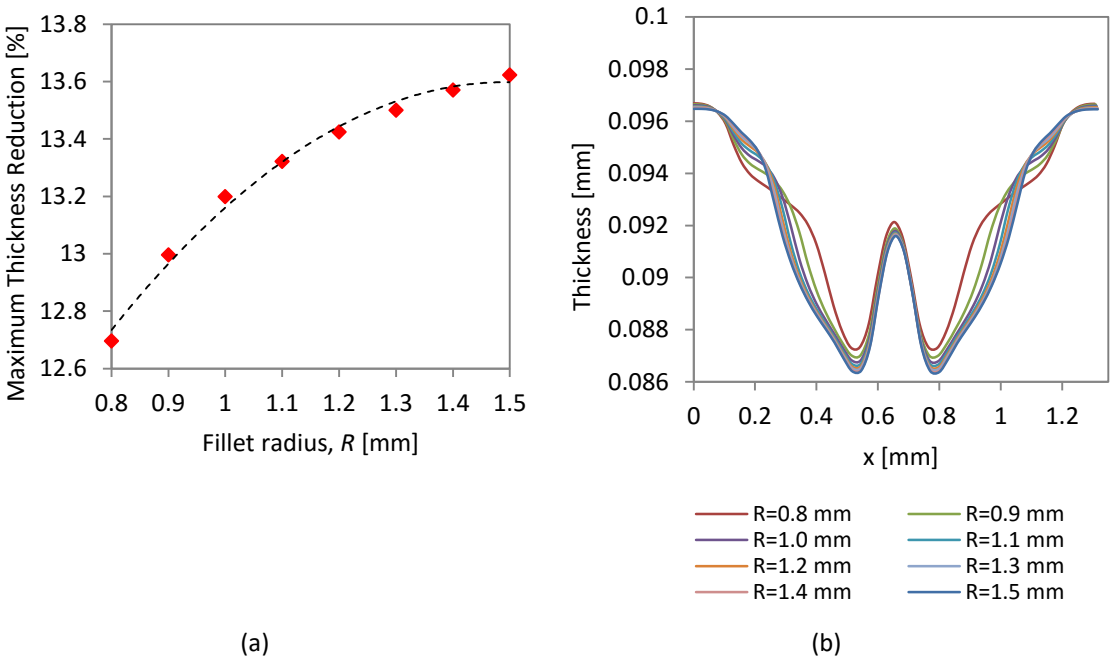

Figure 3.31. Influence of the fillet radius, *R*: (a) Maximum value of thickness reduction, (b) Final thickness distribution.

To evaluate the influence of the main radius on the formability, the remaining parameters are set as shown in Table 3.8.

The main radius starts with 0.55 mm due to the geometry constraints, using an increment of 0.05 mm for each simulation until 30% thickness reduction is obtained. Thus, the range is between 0.2 mm and 0.55 mm, which corresponds to the geometry of the die shown in Figure 3.36 (a) and (b) respectively.

Table 3.8. Tool's geometrical dimensions for the study on the main radius (SS 304).

***w* [mm]**	***s* [mm]**	***h* [mm]**	***R* [mm]**	***r* [mm]**	***a* [mm]**	***t* [mm]**
1.2	1.2	0.4	1.3	0.2 – 0.55	0.2	0.1

(a) (b)

Figure 3.32. Die geometry: (a) Main radius of 0.2 mm, (b) Main radius of 0.55 mm.

Figure 3.33 (a) shows the maximum thickness reduction obtained for different geometries, specially the modification of the main radius. The predicted thickness value decreases with a quadratic tendency. The geometry for a main radius of 0.55 mm is smoother than for a main radius of 0.2 mm, as shown in Figure 3.32. This explains the increase in formability for higher values of the main radius as long as the main radius increases. The comparison between Figure 3.31 (b) and Figure 3.33 (b) allows to conclude that the impact of the main radius is significantly higher than the fillet radius.

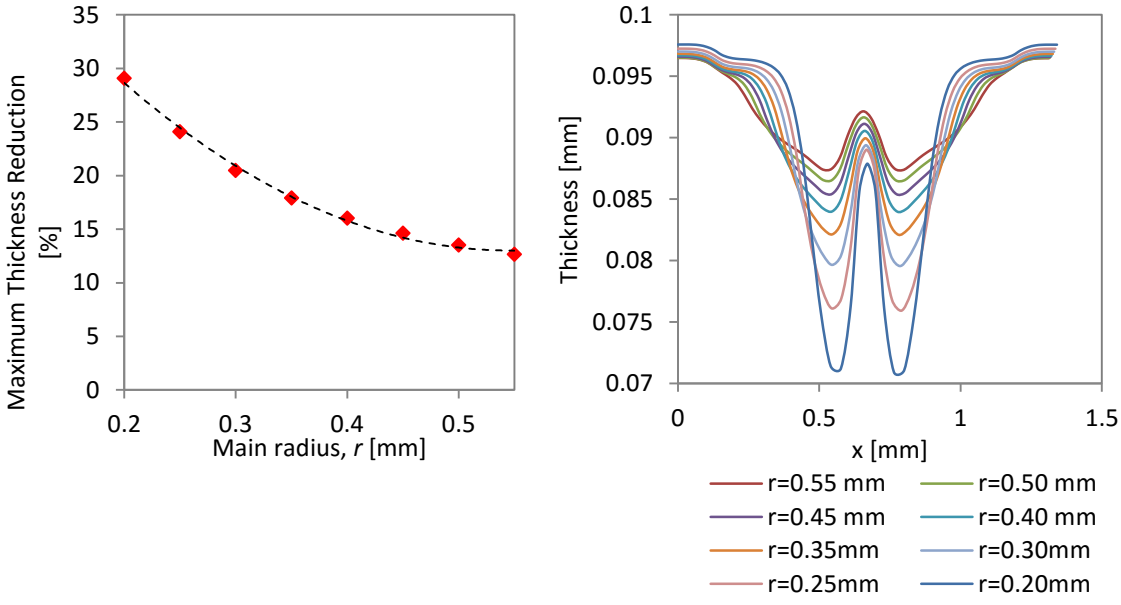

(a) (b)

Figure 3.33. Influence of the main radius, *r*: (a) Maximum thickness reduction, (b) Overall thickness distribution.

The introduction of a new fillet radius onto the geometry removed the previous draft angle as an input variable. Nonetheless, with a tangent line the equivalent draft angle can

still be obtained as shown in Figure 3.34. For an geometry with a channel depth of 0.6 mm and an added radius of 0.8 mm, the draft angle, α (see Figure 2.10), is 48º.

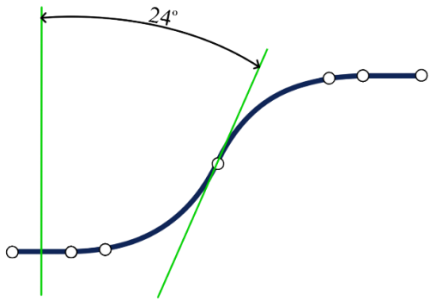

Figure 3.34. Equivalent draft angle, *α*, for the new geometry with an added fillet radius.

To verify the results of the added radius, simulations of the geometry with only one fillet radius were recreated with the draft angle equivalent to the angle obtained with the optimized geometry. For a channel depth of 0.6 mm and a main radius of 0.5 mm the maximum value of plastic strain obtained was 0.462. On the other hand, the optimized geometry with equivalent parameters and a fillet radius of 0.8 mm provides a plastic strain of only 0.395. With a channel depth of 0.5 mm the plastic strain for the geometry with only one fillet radius was 0.35 and for the optimized geometry the plastic strain was 0.30. This study for a channel depth of 0.6 mm is shown in Figure 3.35.

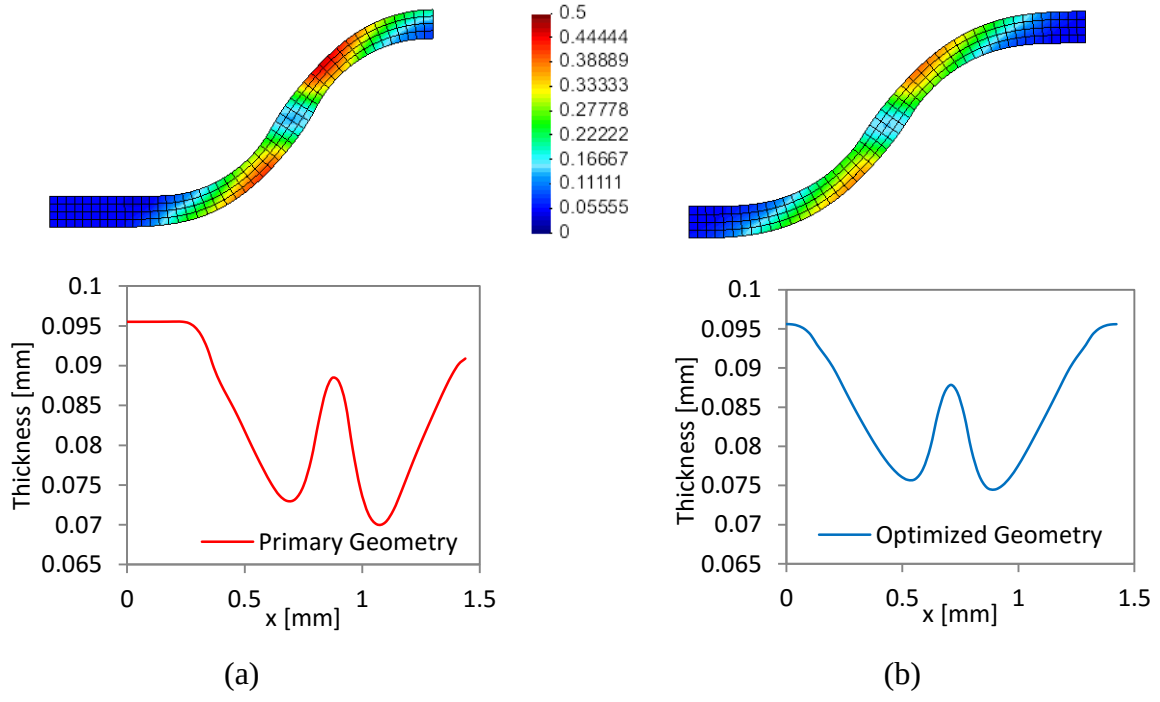

Figure 3.35. Plastic strain and thickness: (a) Primary Geometry, (b) Optimized Geometry.

3.4.4.3. Channel and rib width, *w* and *s* — Flat section, a

To evaluate the influence of the channel and rib width on the formability, the remaining parameters are set as shown in Table 3.9.

Table 3.9. Tool's geometrical dimensions for the study on the channel and rib width (SS 304).

w [mm]	*s* [mm]	*h* [mm]	*R* [mm]	*r* [mm]	*a* [mm]	*t* [mm]
1.2 – 2.4	1.2 – 2.4	0.5	1.3	0.3	0.2 – 1.4	0.1

The channel and rib width start with 1.2 mm and increased with an increment of 0.2 mm until a tendency can be observed. Since the objective is to study the influence of the plane section, the value of *a* must also be increased accordingly with the same increment as the channel and rib dimensions. In this case, the range of the channel and rib width is between 1.2 mm and 3.4 mm and the range for the flat section is between 0.2 mm and 2.4 mm. The geometry of the die for these values is shown in Figure 3.36.

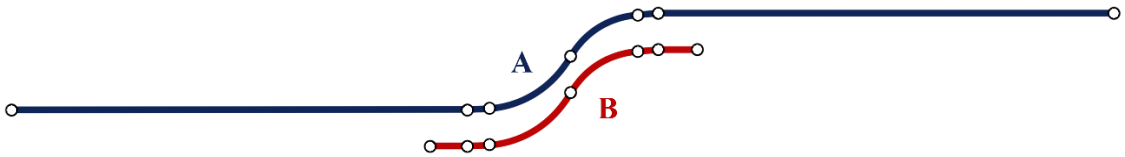

Figure 3.36. Die geometry: (a) Channel and rib width of 3.4 mm, (b) Channel and rib width of 1.2 mm.

Figure 3.37 (a) shows the maximum value of thickness reduction obtained for different channel and rib width. It presents a quadratic decreasing tendency and it is expected to tend to zero for an infinite channel and rib width. The increase in formability was expected due to the increase in material available to flow into the cavity and form the channel.

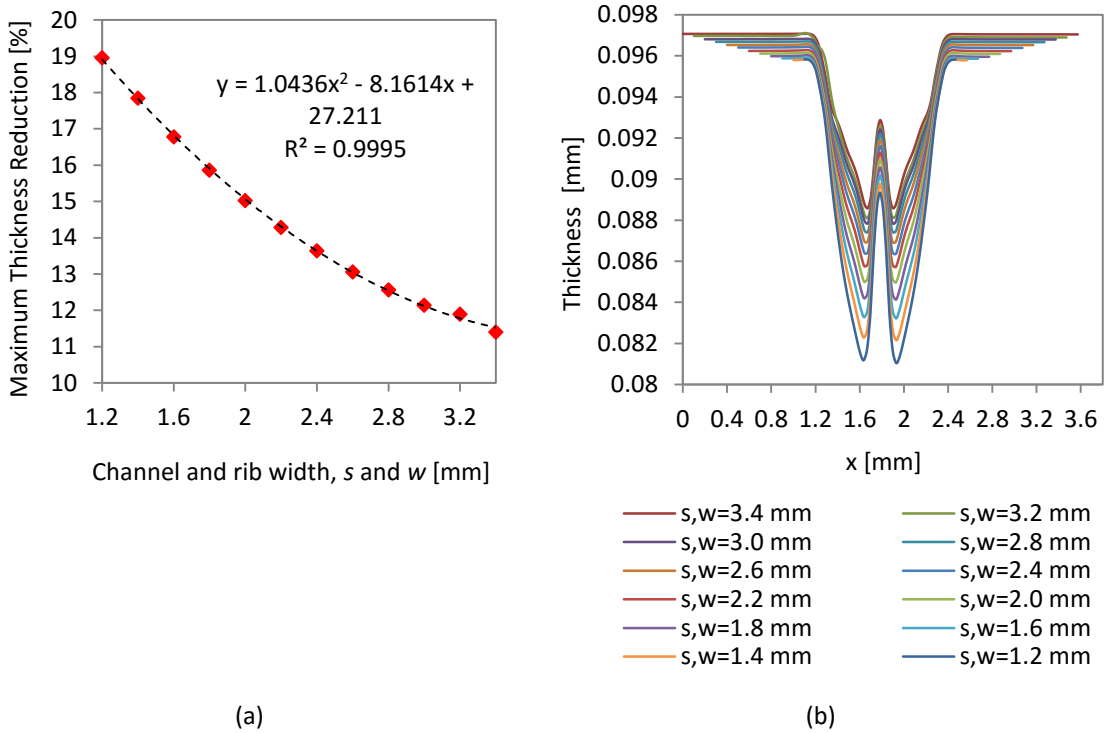

Figure 3.37. Influence of the channel and rib width: (a) Thickness reduction, (b) Overall thickness distribution.

In order to evaluate the influence of the flat section on the formability, the remaining parameters are set as shown in Table 3.10. The flat section starts with 0.2 mm and is increased with an increment of 0.05 mm until the geometry itself prevents further increments. In this case, the range is between 0.2 mm and 0.6 mm and the geometry of the die for these values is shown in Figure 3.38.

Table 3.10. Tool's geometrical dimensions for the study on the flat section (SS 304).

***w* [mm]**	***s* [mm]**	***h* [mm]**	***R* [mm]**	***r* [mm]**	***a* [mm]**	***t* [mm]**
1.2	1.2	0.4	1.3	0.5	0.2 – 0.6	0.1

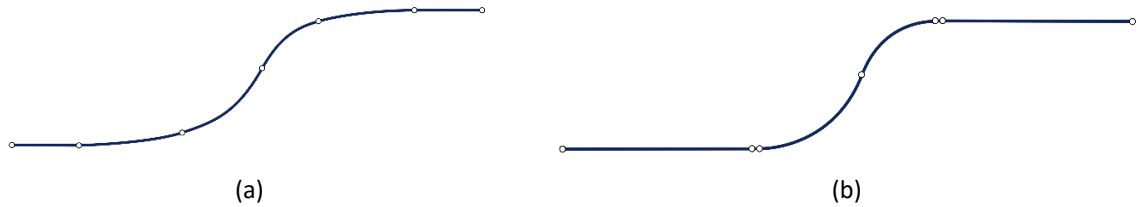

(a) (b)

Figure 3.38. Die geometry: (a) Flat section of 0.2 mm, (b) Flat section of 0.6 mm.

Figure 3.39 (a) shows the maximum value of thickness reduction obtained for different channel geometries. The geometry presented in Figure 3.38 (b) shows the similarity with the first simulations obtained since the fillet radius has nearly no influence on the final geometry. This observation also explains the reduction in formability.

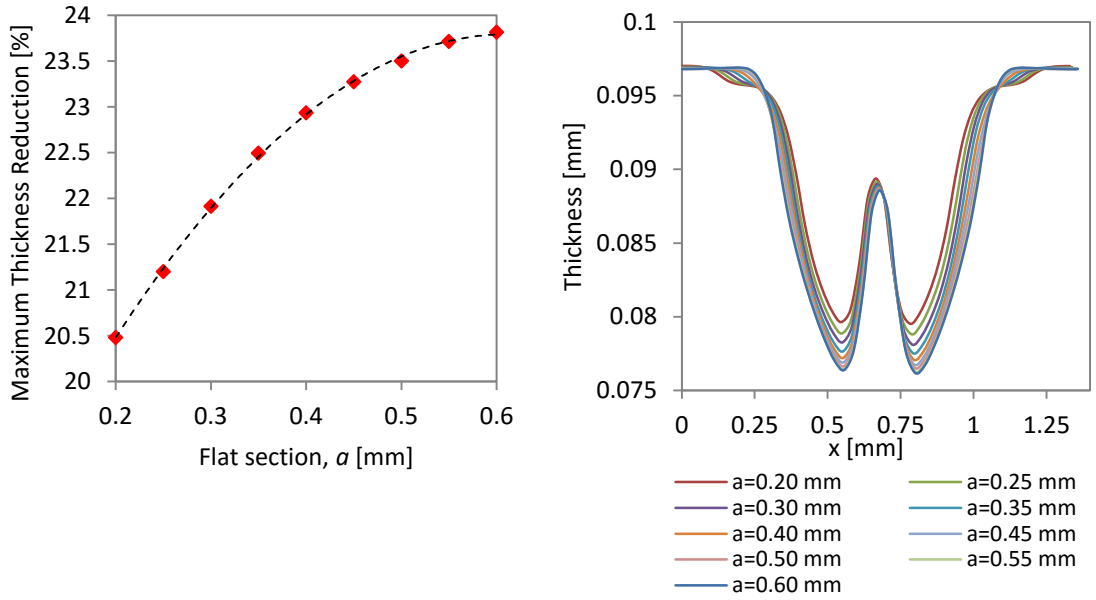

(a) (b)

Figure 3.39. Influence of the flat section, *a*: (a) Thickness reduction, (b) Overall thickness distribution.

3.4.4.4. Blank's initial thickness, *t*.

To evaluate the influence of the blank's initial thickness on the formability, the remaining parameters are set as shown in Table 3.11. The thickness studied varies from 0.05 mm to 0.25 mm, since it is the most used thickness range for stainless steel in metallic bipolar plates. The stainless steel used for the simulations is described for a thickness of 0.1 mm. Thus, the following study must have into account the error committed for using the same

hardening law. Four different thicknesses are studied starting with the blank's initial thickness of 0.05 mm up to 0.25 mm with an increment of 0.05 mm. The results from the extreme values for the simulations can be seen in Figure 3.40.

Table 3.11. Tool's geometrical dimensions for the study on blank's initial thickness (SS 304).

w [mm]	*s* [mm]	*h* [mm]	*R* [mm]	*r* [mm]	*a* [mm]	*t* [mm]
1.2	1.2	0.5	1.3	0.3	0.2	0.05 – 0.25

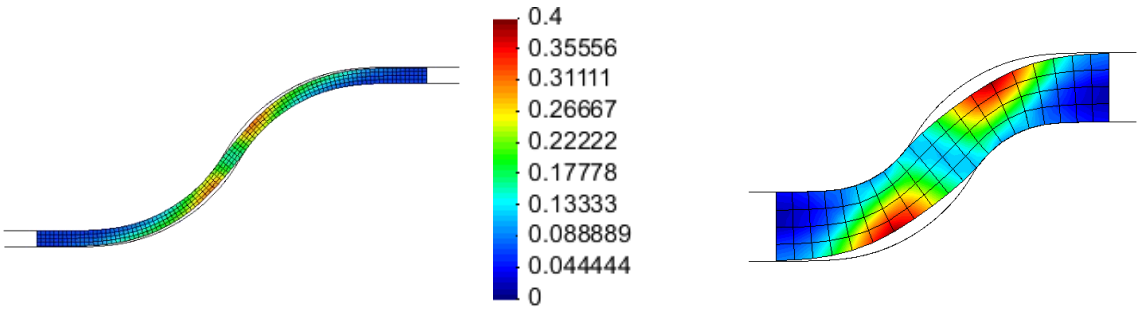

Figure 3.40. Plastic Strain distribution: (a) Initial thickness of 0.05 mm, (b) Initial thickness of 0.25 mm.

Figure 3.41 shows the maximum value of thickness reduction obtained in function of the blank's initial thickness. For all the values of initial thickness, the predicted thickness reduction is approximately identical, except for the 0.05 mm blank. Therefore, a blank's thickness of 0.05 mm is not adequate for a channel depth of 0.5 mm.

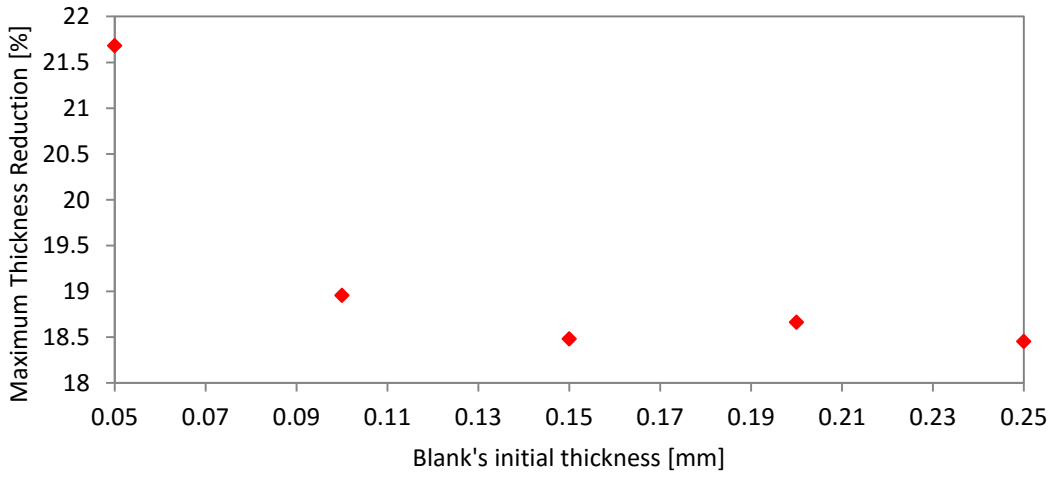

Figure 3.41. Thickness reduction in function on the blank's initial thickness.

The punch force evolution is shown in Figure 3.42 (b) and, as expected, it increases with the increase of the blank's initial thickness. The irregular behaviour in the evolution results from the number of finite elements, as explained on section 3.4.1.

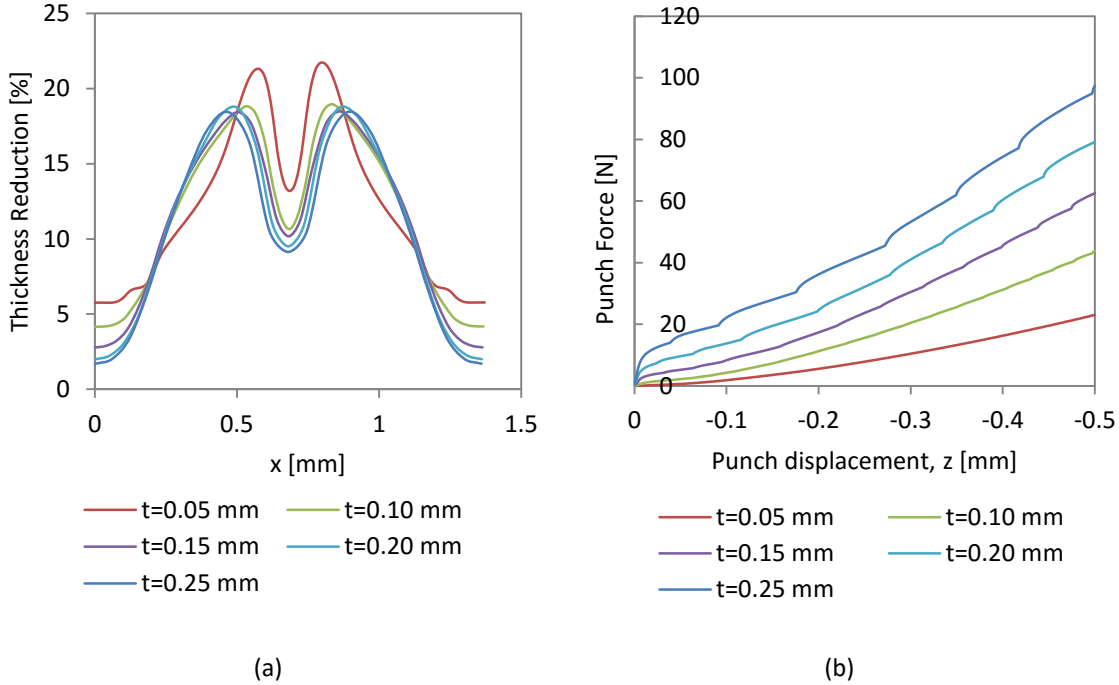

Figure 3.42. Influence of the blank's initial thickness, *t*: (a) Overall thickness distribution, (b) Punch force evolution.

3.4.5. Comparison between Al 1235 and SS304

All numerical simulations performed previously in this study were focused on the stainless steel. After the optimization of the geometry, it is necessary to evaluate the formability for aluminium bipolar plates and compare with the previous results.

Figure 3.43 shows the predicted thickness distribution for the previously used stainless steel SS 304 compared with the aluminium alloy Al 1235. In fact, the aluminium blanks with initial thickness of 0.1 mm have an increased formability compared with stainless steel SS 304. It must be taken in account the mechanical strength obtained from thin aluminium bipolar plates. According to the stress-strain curves presented in Figure 3.2, the punch force required to form the stainless steel is significantly higher than for the aluminium, as shown in Figure 3.44.

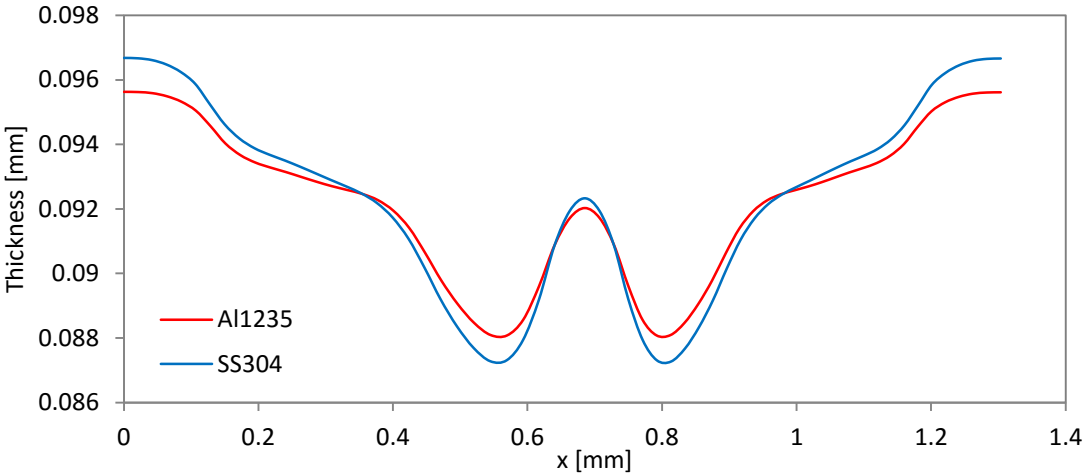

Figure 3.43. Final thickness distribution for stainless steel and aluminium blanks.

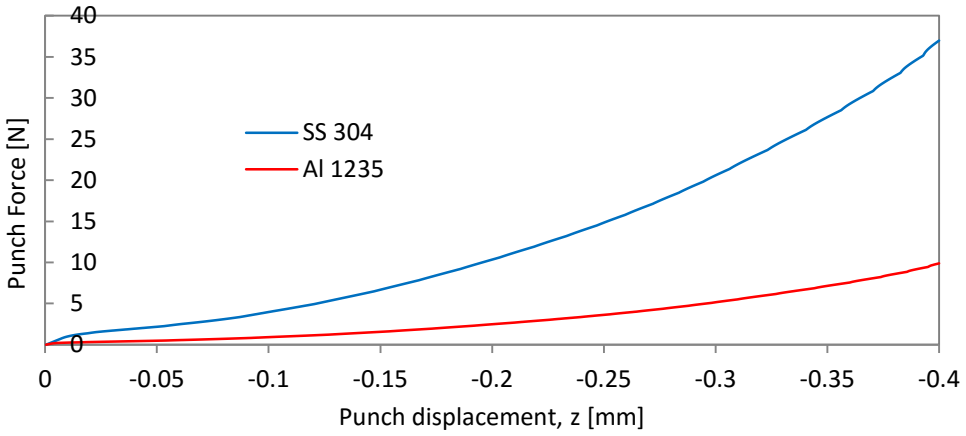

Figure 3.44. Punch force evolution for stainless steel and aluminium blanks.

3.4.6. Study of the curved channel section

After the study of a single straight channel was completed, the next step consists on comparing with the representative zone number 2 of the simplified model, shown in Figure 3.38. This square zone of the blank is discretized with 120 finite elements along the *x* and *y* directions and five along the thickness while the representation of the tools is shown in Figure 3.7 (b). To compare adequately both numerical results, a mirror has been applied on the 2D simulation (see Figure 3.46 (a)).

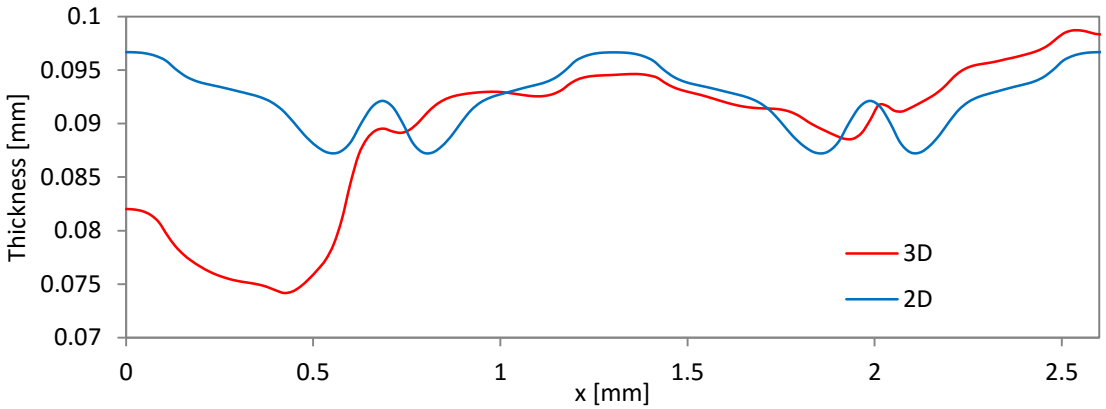

Figure 3.45. Thickness reduction for 2D and 3D simulations.

The results for the curved section show an increase in thickness reduction compared with the straight channel section, as shown in Figure 3.45. This behaviour is explained since only plane strain deformation occurs in the 2D model and the 3D model presents a deformation along every orientation with a curved geometry.

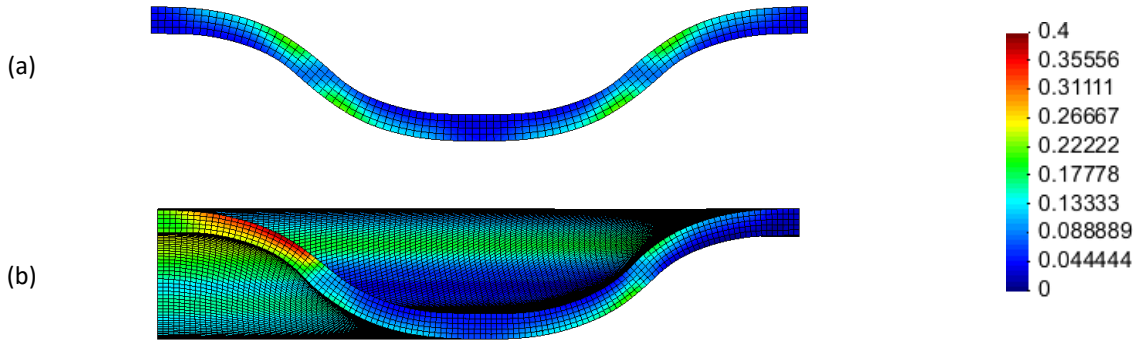

Figure 3.46. Plastic strain distribution: (a) 2D simulation, (b) 3D simulation.

The comparison of the plastic strain for both the 2D and 3D simulation is shown in Figure 3.46. The 2D simulation has a maximum plastic strain of 0.22 while the 3D simulation has a maximum plastic strain of 0.38. The maximum plastic strain for the 3D simulation occurs in the fillet radius closer to the revolution axis, since the radius of the curvature is inferior than for the fillet radius represented on the right side of Figure 3.46 (b). Since the 2D model does not represent a curved section of the flow channel, the plastic strain distribution is symmetric.

The simulation of the curved section using boundary conditions to restrain the four sides represents the most disadvantageous situation in terms of forming. In order to verify the influence of the straight channel on the curved section, a comparison between a 3D

simulation with only the curved section and a 3D simulation with the curved section with the straight channel is carried out. The number of finite elements used for the curved section is 120 for the *x* and *y* directions and for the straight channel a progressive mesh was used (see Figure 3.47 (a)) with 100 elements along the straight channel. This model presents four finite elements along the thickness.

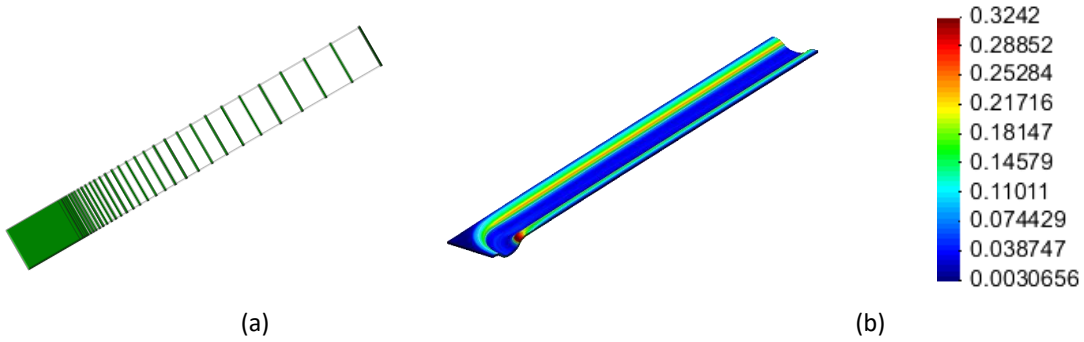

(a) (b)

Figure 3.47. (a) Progressive mesh, (b) Plastic strain distribution for the curved section with the straight channel.

The comparison between both simulations is shown in Figure 3.48. Although the results are similar, the curved section with the influence of the straight channel clearly demonstrates lower deformation, as shown in Figure 3.48. In fact, the minimum thickness is 0.080 mm using the straight channel, while without the straight channel the minimum thickness is 0.074 mm.

The blank of the 2D simulation contains only 192 nodes, resulting in a simulation of 52 seconds (CPU Time: 357 seconds). When running a 3D simulation, the simulation time increases drastically. The 3D model presents 72000 nodes with a computational time of 8 hours 43 minutes and 57 seconds (CPU Time: 179580 seconds). Adding the channel, even with less finite elements along the thickness, increases the number of nodes to 105600 corresponding to a simulation time of 14 hours 12 minutes and 30 seconds (CPU Time: 289111 seconds).

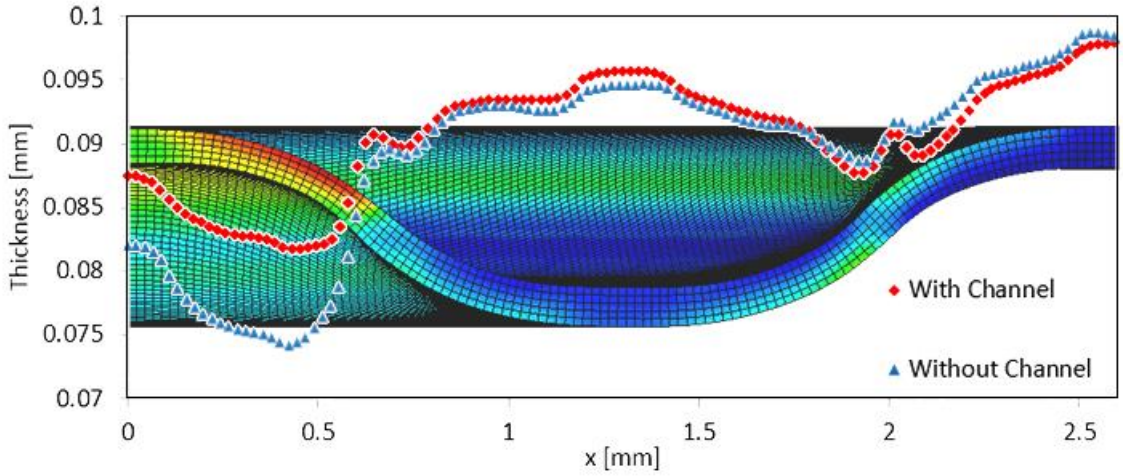

Figure 3.48. Final thickness for the curved section with and without the straight channel.

3.5. Hydroforming

In section 2.3 different forming processes were discussed. This study focused on the microstamping process, but there is a need to evaluate the remaining forming processes to verify the eventual benefits. This section focuses on the comparison between microstamping and hydroforming processes.

The hydroforming simulation only requires the die and the application of pressure on the other side of the blank to create de desired shape. This pressure has to be enough to allow the blank to accommodate the desired shape but low enough to avoid an increased in thickness reduction.

The process is divided in two phases: first the die is maintained stationary while a pressure is applied to the blank to form the desired shape. This phase ends when the selected pressure is attained. The second phase is the removal of the pressure in a single instant for the springback effect to occur.

The following simulations use the optimized geometry obtained with microstamping with the same boundary conditions in order to compare adequately the results. Hence, the tool geometry used has the dimensions in Table 3.12. The initial thickness of 0.1 mm for stainless steel is used along with four finite elements along the blank's thickness.

Table 3.12. Tool's geometrical dimensions for the study of hydroforming (SS 304).

w [mm]	*s* [mm]	*h* [mm]	*R* [mm]	*r* [mm]	*a* [mm]	*t* [mm]
1.2	1.2	0.4	0.8	0.5	0.2	0.1

The first step consists in verifying the pressure required for the geometry used. Simulations were performed varying the pressure from 50 MPa to 400 MPa with an increment of 50 MPa. The results for the simulations with a pressure of 50 MPa and 400 MPa are shown in Figure 3.49.

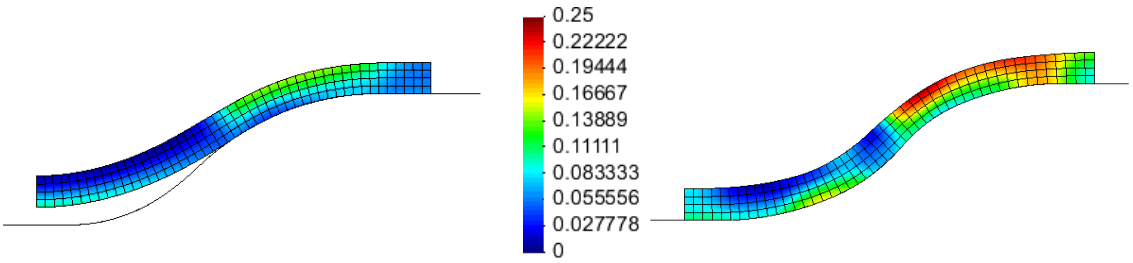

Figure 3.49. Plastic strain distribution for (a) Hydroforming with *p* = 50 MPa, (b) Hydroforming with *p* = 400 MPa.

For the geometry tested, with a pressure above 100 MPa, the simulations have similar results, when comparing the final desired geometry. Only a slight improvement is obtained with a pressure of 300 MPa. The simulation with 50 MPa presents inferior results in terms of final geometry obtained

The thickness reduction obtained for different pressures is shown in Figure 3.50. The thickness reduction for hydroforming using forming pressures from 100 MPa up to 300 MPa is under 13.5 %. On the other hand, increasing the pressure above 300 MPa induces an increase in thickness reduction, while pressures of 50 MPa do not achieve the geometrical objective.

The thickness reduction obtained with microstamping, for the same geometry, is under 13% which represents better results than the simulations for the hydroforming process.

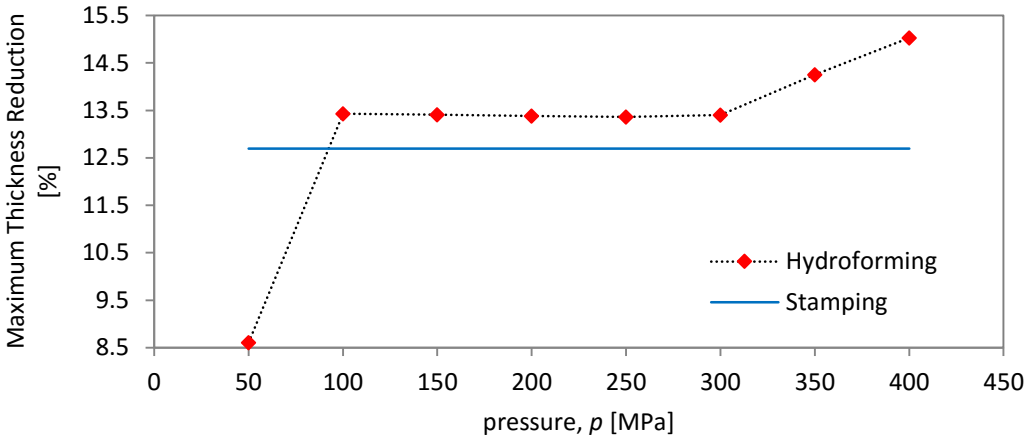

Figure 3.50. Thickness reduction for hydroforming with pressure from p = 50 MPa to p = 400 MPa.

The thickness distribution for hydroforming at different levels of pressure is shown in Figure 3.51. The increase in pressure induces an increase in the maximum thickness reduction since its maximum is for a pressure of 400 MPa.

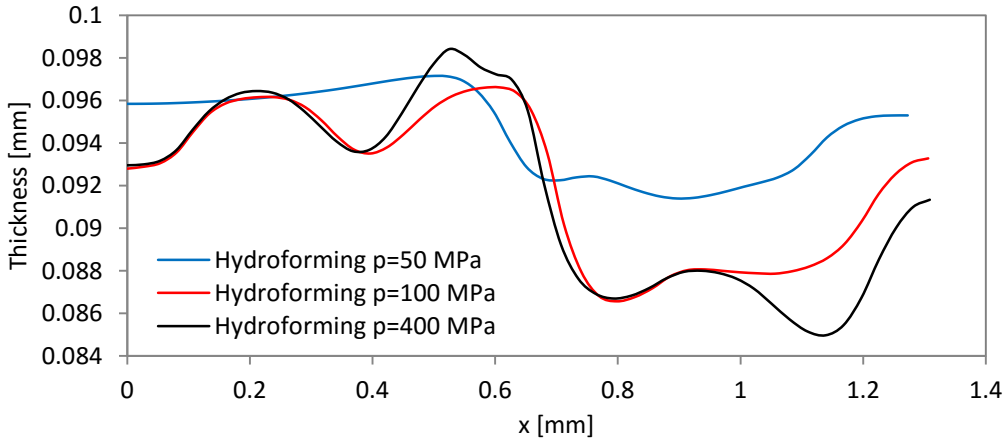

Figure 3.51. Thickness distribution for hydroforming for pressures from 50 MPa to 400 MPa.

Observing the results for the hydroforming process shown in Figure 3.49, with a symmetric geometry, the highest values of plastic strain are displayed in the first section of contact between the blank and the die. With this behaviour, the following simulation tries to increase the plastic strain where the values are lower in order to reduce the plastic strain on the critical radius. This can be achieved by increasing the radius of the critical point, while reducing the one on the bottom of the channel. The new geometry compared with the previous symmetric one is shown in Figure 3.52.

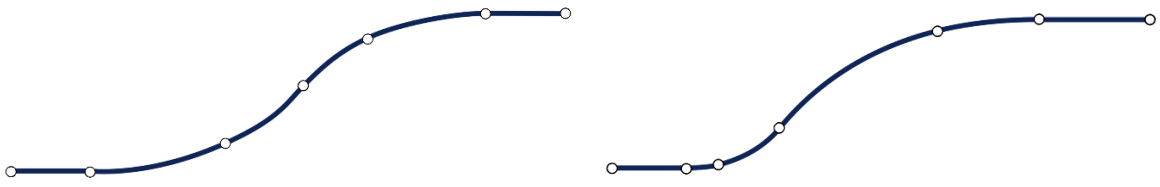

(a) (b)

Figure 3.52. Die geometry (a) Symmetric optimal geometry for microstamping, (b) Hydroforming geometry.

The comparison between the symmetric geometry and the new geometry for a pressure of 250 MPa is shown in Figure 3.53, presenting a plastic strain distribution plotted on the deformed geometry. The maximum plastic strain for the new geometry occurred in a different location compared with the symmetric geometry, with a similar value for the maximum plastic strain obtained.

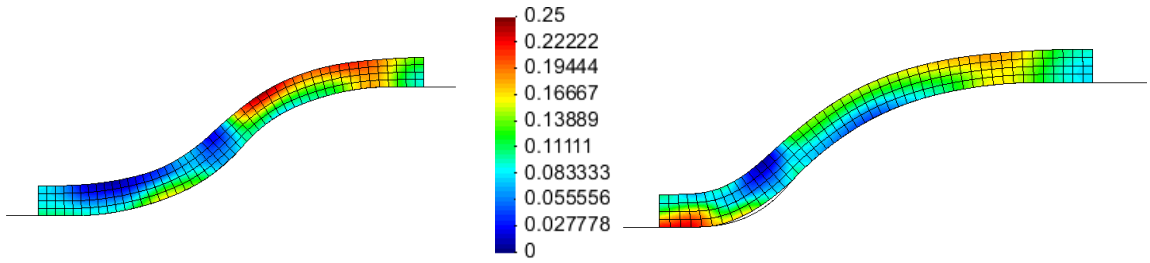

(a) (b)

Figure 3.53. Plastic strain for a pressure of 250 MPa for hydroforming: (a) Symmetric Geometry, (b) New Geometry.

The thickness distribution along the blank for microstamping and hydroforming with the different geometries is shown in Figure 3.54. Even though the maximum plastic strain occurred in a different location, the maximum thickness reduction for both numerical simulations still occurred on the same fillet radius and with similar results.

The new geometry improves the results in regard of plastic strain and with a decrease in thickness reduction, but all the results obtained from hydroforming show results inferior to microstamping.

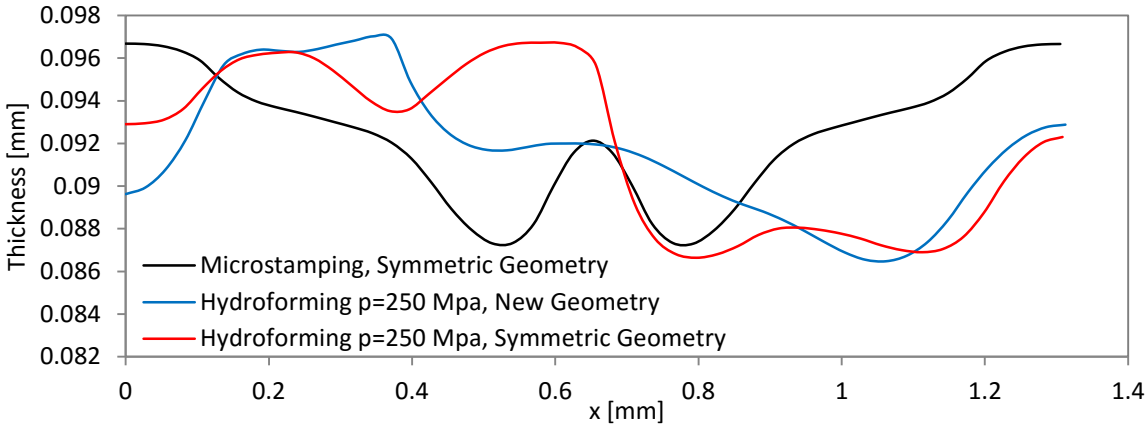

Figure 3.54. Thickness distribution for hydroforming and microstamping.

3.6. Results and Discussion

Liu et al. (2010) studied the deformation on metallic bipolar plates with the rubber pad forming process. The main study consisted on the formation of a 1.2 mm channel with 0.6 mm of depth. The best results obtained for a concave deformation style were with a maximum value of stress of 642.5 MPa as shown in Figure 3.55.

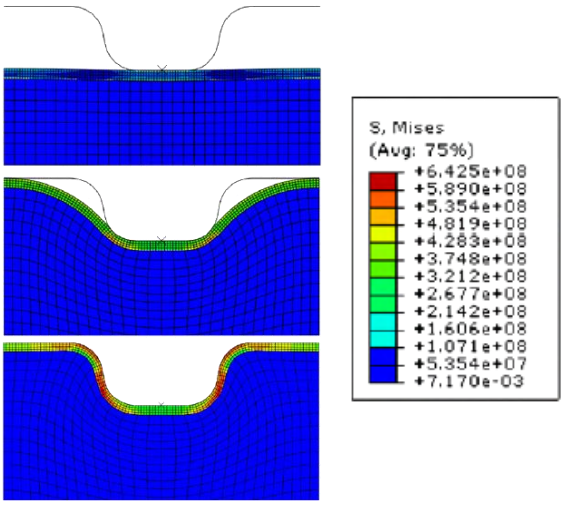

Figure 3.55. Stress values for rubber pad forming process (Liu et al., 2010).

For the optimized geometry obtained with this study, it was possible to obtain greater results. With a fully constrained model, recreating the channels in the worst conditions of the bipolar plate, it was possible to obtain a maximum value of stress of around 700 MPa for

a similar geometry with a channel width of 1.2 mm and a channel depth of 0.6 mm. But, if the boundary conditions used by Liu et al. 2010 were replicated with the added material on one extremity, the maximum value of stress drops to 556 MPa, as shown in Figure 3.56. Note that the added material on one extremity will not affect the results since the extremity is free to move.

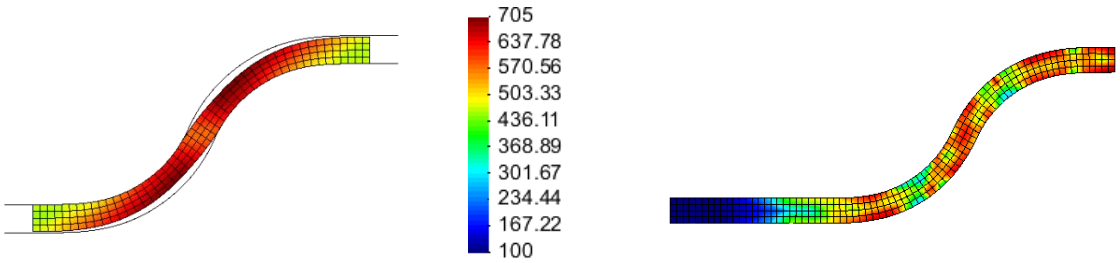

Figure 3.56. Stress values: (a) fully constrained finite element model, (b) free on one extremity finite element model.

The plastic strain for the simulations shown in Figure 3.56 is shown in Figure 3.57, which demonstrates the influence of the boundary conditions on a finite element model.

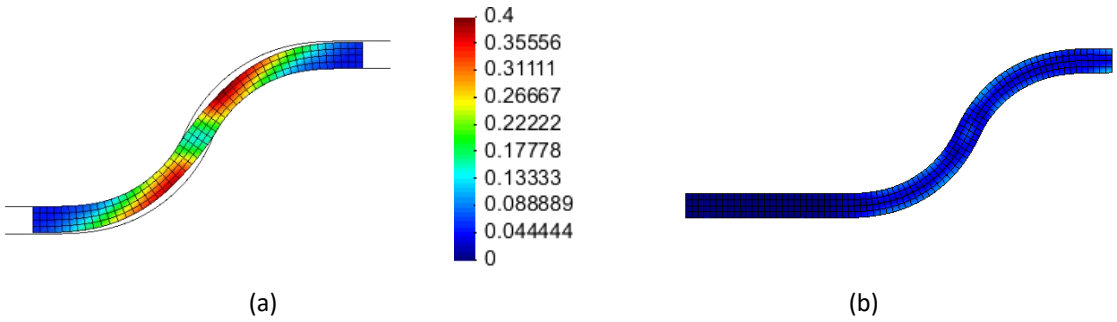

Figure 3.57. Plastic strain: (a) fully constrained finite element model, (b) free on one extremity finite element model.

In sum, for similar conditions as previous studies, the optimized geometry has an improved formability but the fully constrained model has to be taken into account due to the accurate representation of the channels from the centre of the metallic bipolar plate.

4. CONCLUSIONS

This study presented the finite element simulation of the forming process used to manufacture metallic bipolar plates. The objective was to improve the formability by optimizing the geometry of the flow channels, selecting the optimal material and stamping process.

All the numerical simulations were performed with the in-house finite element code DD3IMP. Different materials were considered in this study, namely the stainless steel SS 304 and two aluminium alloys (Al 5042 and Al 1235). The evolution of the yield surface was described by two hardening laws: Swift law and Voce law, depending on the material selected. Regarding the yield criterion, the material is assumed isotropic in all simulations (von Mises). The constitutive parameters required for the hardening law were obtained from the studies carried out by other authors.

Since the geometry of a bipolar plate contains several geometrical details with very small fillet radiuses, the numerical simulation of the entire bipolar pate involves a huge computational cost. Therefore, in the presented study, representative zones were selected and analysed in detail. The first one was the study of a single channel, allowing to perform numerical simulations in 2D conditions (plane strain deformation). The second important zone represented the curved section of the flow channel on the bipolar plate, where 3D simulations were required. This simplification in the forming process required adequate boundary conditions to represent accurately the physical process. Thus, different boundary conditions were applied, covering the different situations. The first situation is when the flow channel is closer to the edge of the bipolar plate, i.e. the edges are free of constraints. On the other hand, the second situation is when considering a channel with the edges completely constrained. The thickness reduction was larger in the second situation, but the thickness distribution was more uniform, providing a better contact between each flow channel and the membrane. The most disadvantageous situation (second one) was chosen for this study, which represents a central channel fully constrained.

In order to optimize the geometry of the forming tools used to produce the bipolar plates, a parametric model was created using CATIA®V5. The geometry of a single channel was described by seven variables in the parametric model, allowing to build a wide range of

geometries to be used in the finite element simulation. Therefore, the influence of each geometrical parameter was evaluated in order to increase the formability of the blank. Seven parameters were tested:

- The first parameter to be tested was the channel depth, *h*. The thickness reduction increased with the increase of the channel depth. The maximum value of thickness reduction followed a quadratic crescent tendency as the channel depth was increased. It was possible to reach a channel depth of 0.65 mm with a maximum thickness reduction of 30%. The increase in channel depth led to an increase in punch force.
- The second parameter was the added fillet radius, *R*. The thickness reduction increased with the increase of the fillet radius. Once again, observing the maximum thickness reduction for each simulation, it was clear that it followed a quadratic crescent tendency as the fillet radius increased. The best results were observed for an added fillet radius of 0.8 mm which corresponds to a maximum thickness reduction of 12.7%. The main fillet radius, *r*, was also studied. When the main fillet radius increased, the thickness reduction decreased with a quadratic tendency. The best results were observed for a main fillet radius of 0.5 mm (maximum thickness reduction under 15%).
- The next parameter studied was a plane section of the cross-section of the straight channel. To evaluate such section, both the rib, *s*, and channel width, *s*, were increased to maintain the symmetry, as well as the flat section, *a*. With the straight section increased, the maximum thickness reduction decreased with a quadratic tendency.
- In order to keep the channel and rib width, the next parameter analysed was the flat section, *a*. Increasing this parameter without altering the channel and rib width, the arc length of the fillet radius changed, reducing the formability of the blank. Increasing the flat section to 0.6 mm induced a maximum thickness reduction of 23.7%.
- The last parameter was the blank's initial thickness, *t*. For stainless steel, an initial thickness of 0.05 mm led to a maximum thickness reduction of 21.7%, while for further values of thickness the maximum thickness reduction was similar for each simulation with values between 18.5% and 19%.

Considering the 2D simulation of a single channel, the comparison between stainless steel SS 304 and aluminium alloy Al 1235 was performed. Maintaining the blank's initial thickness of 0.1 mm, the aluminium presented higher formability in comparison with stainless steel, being the improvement of around 2%. For the same geometry, the straight and curved section of the flow channel presented a maximum plastic strain of 0.22 and 0.39, respectively. The influence that the straight section of the flow channel has on the curved section was analysed. The maximum plastic strain decreased from 0.4 to 0.32.

Finally, the influence of the stamping process was evaluated by comparing the microstamping and the hydroforming processes. Comparing both forming processes with the same geometry, the microstamping process provides better results in terms of formability. Applying a pressure between 100 MPa and 300 MPa in the hydroforming process, the maximum thickness reduction was 13.5%, compared with 12.5% obtained in the microstamping process. Further values of pressure increase the maximum thickness reduction, while a pressure of 50 MPa did not achieve the geometrical objective for the blank, since it presented lack of contact between the blank and the die. Since the optimal geometry can be different depending on the forming process, an attempt in changing the geometry was performed, improving the results for hydroforming, but sill presenting inferior results compared with microstamping.

5. REFERENCES

A.Heinzzel, University of Duisburg-Essen, Duisburg, G., F. Mahlendorf, University of Duisburg-Essen, Duisburg, G., C. Jansen, University of Duisburg-Essen, Duisburg, G., 2009. Bipolar Plates. Elsevier 810–816.

Belali-Owsia, M., Bakhshi-Jooybari, M., Hosseinipour, S.J., Gorji, A.H., 2014. A new process of forming metallic bipolar plates for PEM fuel cell with pin-type pattern.

Carrette, L., Friedrich, K. a, Stimming, U., 2001. Fuel Cells - Fundamentals and Applications. Fuel Cells 1, 5–39.

Hadi, S., 2014. Micro deep drawing of Aluminium foils AA1235. University of Wollongong.

Holton, O.T., Stevenson, J.W., 2013. The Role of Platinum in Proton Exchange Membrane Fuel Cells. Platin. Met. Rev. 57, 259–271.

Hu, P., Peng, L., Zhang, W., Lai, X., 2009. Optimization design of slotted-interdigitated channel for stamped thin metal bipolar plate in proton exchange membrane fuel cell. J. Power Sources 187, 407–414.

Hu, Q., Zhang, D., Fu, H., 2015. Effect of flow-field dimensions on the formability of Fe-Ni-Cr alloy as bipolar plate for PEM (proton exchange membrane) fuel cell. Energy 83, 156–163.

Hughes, T.J.R., 1980. Generalization of selective integration procedures to anisotropic and nonlinear media. Int. J. Numer. Methods Eng. 15, 1413–1418.

Li, X., Sabir, I., 2005. Review of bipolar plates in PEM fuel cells: Flow-field designs. Int. J. Hydrogen Energy 30, 359–371.

Liu, Y., Hua, L., 2010. Fabrication of metallic bipolar plate for proton exchange membrane fuel cells by rubber pad forming. J. Power Sources 195, 3529–3535.

Liu, Y., Hua, L., Lan, J., Wei, X., 2010. Studies of the deformation styles of the rubber-pad forming process used for manufacturing metallic bipolar plates. J. Power Sources 195, 8177–8184.

Mahabunphachai, S., Necati, Ö., Koc, M., 2010. Effect of manufacturing processes on formability and surface topography of proton exchange membrane fuel cell metallic bipolar plates 195, 5269–5277.

Menezes, L.F., Teodosiu, C., 2000. Three-dimensional numerical simulation of the deep-

drawing process using solid finite elements. J. Mater. Process. Technol. 97, 100–106.

Msolli, S., Martiny, M., Cardoso, M.C., Moreira, L.P., Mercier, S., Molinari, A., 2016. Numerical modeling of the deformation of AISI 304L using a tangent additive Mori-Tanaka homogenization scheme: Application to sheet metal forming. J. Mater. Process. Technol. 235, 187–205.

Neto, D.M., 2014. Numerical simulation of frictional contact problems using Nagata patches in surface smoothing 350.

Neto, D.M., Oliveira, M.C., Dick, R.E., Barros, P.D., Alves, J.L., Menezes, L.F., 2015. Numerical and experimental analysis of wrinkling during the cup drawing of an AA5042 aluminium alloy. Int. J. Mater. Form.

Neto, D.M., Oliveira, M.C., Menezes, L.F., Alves, J.L., 2014. Applying Nagata patches to smooth discretized surfaces used in 3D frictional contact problems. Comput. Methods Appl. Mech. Eng. 271, 296–320.

Neto, D.M., Oliveira, M.C., Menezes, L.F., Alves, J.L., 2013. Improving Nagata patch interpolation applied for tool surface description in sheet metal forming simulation. Comput. Des. 45, 639–656.

Oliveira, M., Alves, J., Chaparro, B., Menezes, L., 2007. Study on the influence of work-hardening modeling in springback prediction. Int. J. Plast. 23, 516–543.

Park, W.T., Jin, C.K., Kang, C.G., 2016. Improving channel depth of stainless steel bipolar plate in fuel cell using process parameters of stamping. Int. J. Adv. Manuf. Technol.

Peng, L., Yi, P., Lai, X., 2014. Design and manufacturing of stainless steel bipolar plates for proton exchange membrane fuel cells. Int. J. Hydrogen Energy 39, 21127–21153.

Smith, T.L., Santamaria, A.D., Park, J.W., Yamazaki, K., 2014. Alloy Selection and Die Design for Stamped Proton Exchange Membrane Fuel Cell (PEMFC) Bipolar Plates. Procedia CIRP 14, 275–280.

Son, C.-Y., Jeon, Y.-P., Kim, Y.-T., Kang, C.-G., 2012. Evaluation of the formability of a bipolar plate manufactured from aluminum alloy Al 1050 using the rubber pad forming process. Proc. Inst. Mech. Eng. Part B J. Eng. Manuf. 226, 909–918.

Tawfik, H., Hung, Y., Mahajan, D., 2007. Metal bipolar plates for PEM fuel cell-A review. J. Power Sources 163, 755–767.

Wang, Y., Chen, K.S., Mishler, J., Cho, S.C., Adroher, X.C., 2011. A review of polymer electrolyte membrane fuel cells: Technology, applications, and needs on fundamental

research. Appl. Energy 88, 981–1007.

Yi, P., Du, X., Kan, Y., Peng, L., Lai, X., 2015. Modeling and experimental study of laser welding distortion of thin metallic bipolar plates for PEM fuel cells. Int. J. Hydrogen Energy 40, 4850–4860.

Yoon, W., Huang, X., Fazzino, P., Reifsnider, K.L., Akkaoui, M.A., 2008. Evaluation of coated metallic bipolar plates for polymer electrolyte membrane fuel cells. J. Power Sources 179, 265–273.

Zhou, T.-Y., Chen, Y.-S., 2015. Effect of Channel Geometry on Formability of 304 Stainless Steel Bipolar Plates for Fuel Cells—Simulation and Experiments. J. Fuel Cell Sci. Technol. 12, 051001.

APPENDIX A

The following page presents a guide to create a parametric model with CATIA®V5 as used for the presented work.

Create a Parametric Model with CATIA

Works for:

- Part Design
- Generative Shape Design

1

- The first step is to open CATIA V5
- Click *Insert* → *New Part*

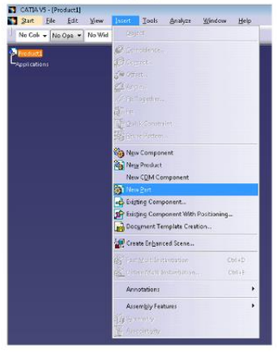

2

- Double click on the desired plane

- Click and draw the sketch with th aproximate dimensions of the model
- Create the desired model including all the extrudes, cuts, etc...

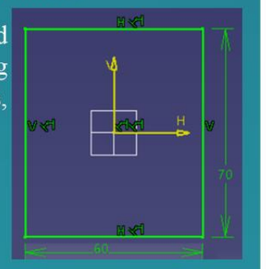

3

- Make sure the Product is selected on the Tree by double clicking on it to turn it to blue

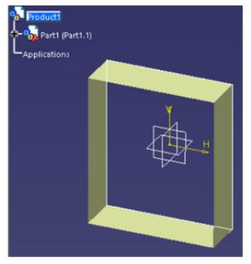

- Click on *Formula* from the toolbars

4

- Select the type of parameter (Length, Angle, etc..) according to the selected parameter. For most geometrical dimensions (length, radius, etc..), select *Length* and click on *New Parameter of type*

- Edit the new parameter's name and change the value to be similar to the value previously chosen

5

- On the list of parameters, find and select the dimension to intdoduce as a variable

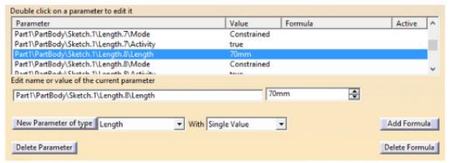

- Click on *Add Formula*

6

- On *Members of Parameters*, select *Renamed Parameters* to easily find the parameter previously created

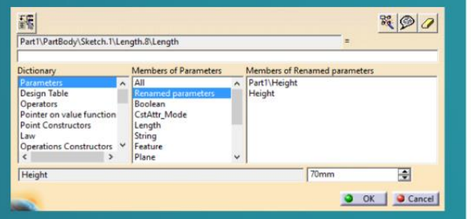

7

- Choose the correspondent variable to associate with the dimension selected
- Double click on the variable to introduce in the equation

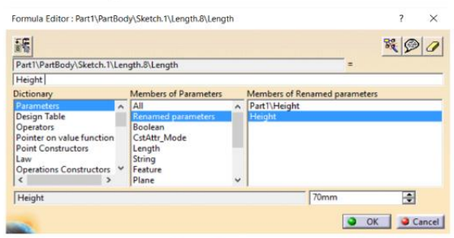

- Repeat steps 4 to 7 for each parameter

8

- Click on *Design Table*

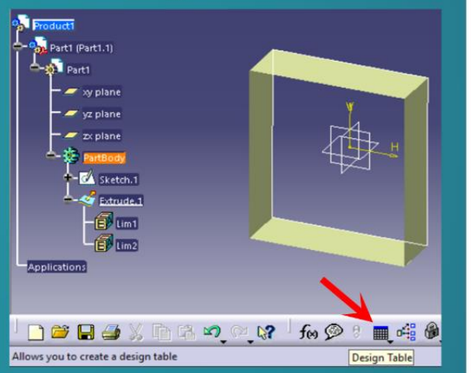

9

- Select *Create a design table with current parameter values*
- Choose the orientation desired for Excel

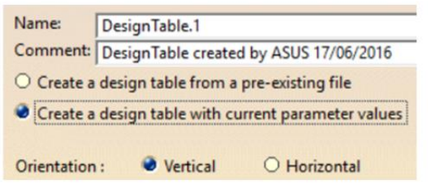

- Click OK

10

- Look for the desired parameters on the list
- Filter by *Renamed Parameter* type to help on finding the variable parameter

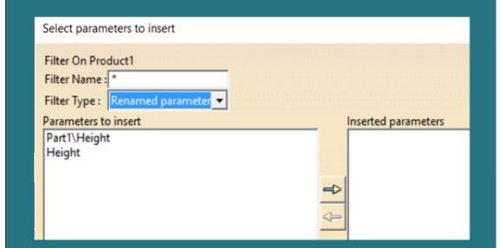

11

- Select all the parameters to add to Excel and click

- Click OK
- Save the design table

12

- Open the Excel document and change the value of the parameters to the desired value whenever needed
- Save the Excel document and go back to the CAD design

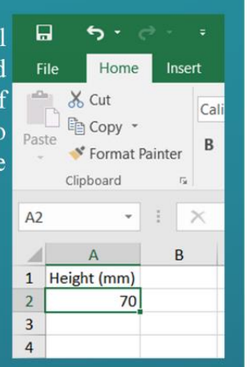

13

- Close the *Knowledge Report*
- Whenever a surface from the model turns to red, the model requires an uptade
- With the product selected on the Tree, click to update

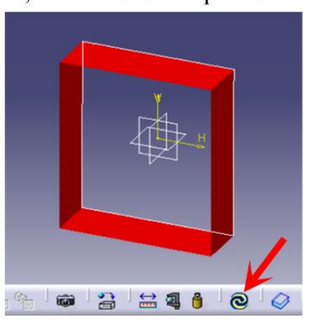

14

- This is it! The model has now changed to the values inserted in the previously created Excel document and can be changed at any time

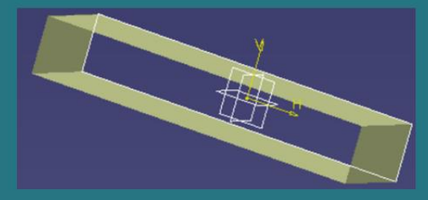

APPENDIX B

Paper currently in final preparation for submission.

Numerical simulation of the stamping process of stainless steel bipolar plates and channel geometry optimization

Nicolas Marques, Diogo Neto

ABSTRACT: A bipolar plate is one of the key components of proton exchange membrane fuel cells, which are considered as potential power sources for transportation and portable applications. The main objective of this paper is the optimization of the stamping process of stainless steel SS 304 bipolar plates for PEM fuel cells with the use of numerical models in the simulation of a deep drawing process. The numerical simulations presented in this paper were carried out with the in-house finite element code DD3IMP. The geometry of the flow field has a large influence on the formability during the stamping process. Therefore, the aim of the paper is to study the different geometrical variables in order to optimize the flow channel dimensions. Accordingly, a parametric CAD model containing the stamping tools' geometry is created, which is posteriorly used in the simulation with a finite element method. The simplified model is used to study the deformation behaviour found in the plate such as a 2D analysis (plane strain deformation) to evaluate the straight channel. The numerical results shown that increasing the main radius, the channel width and the rib width and diminishing the channel depth, the fillet radius and the flat section the formability of the blank is improved

1 INTRODUCTION

In the last decades there has been an increasing concern about environmental consequences on the use of fossil fuel for electricity production and vehicle propulsion. Sustainable energy became important with the increase in population since common sources of energy have poisonous emissions into the atmosphere[1].

In order to reduce the dependence on fossil fuels and diminish poisonous emissions, renewable energy from wind, water and sun were already implemented. Nevertheless, these sources are irregularly available thus not being suited to cover all electrical needs[1].

An option for future power generations are fuel cells, which use pure hydrogen and producing only water eliminating all local emissions [1].

Fuel cells are electrochemical devices that convert chemical energy stored in fuels into electrical energy [2].

The fuel cells can be categorised in five main categories: polymer electrolyte membrane fuel cells (PEMFC), solid oxide fuel cells (SOFC), alkaline fuel cells (AFC), phosphoric acid fuel cells (PAFC) and molten carbonate fuel cells (MCFC). For transportation an portable applications, PEM fuel cells are promising candidates since they gather the most important characteristics for such applications [3].

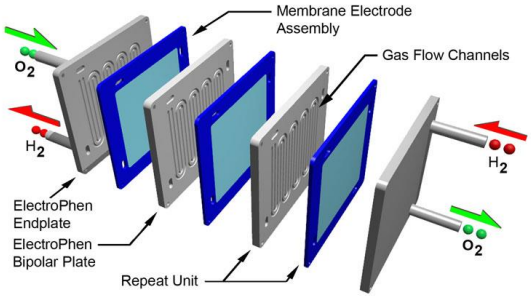

Figure 1.1. *Proton exchange membrane fuel cell (PEMFC) assembly [2].*

Fuel cells are composed by different components assembled in stacks as shown in Figure 1.1. Each stack consists of a membrane electrode assembly and bipolar plates [4].

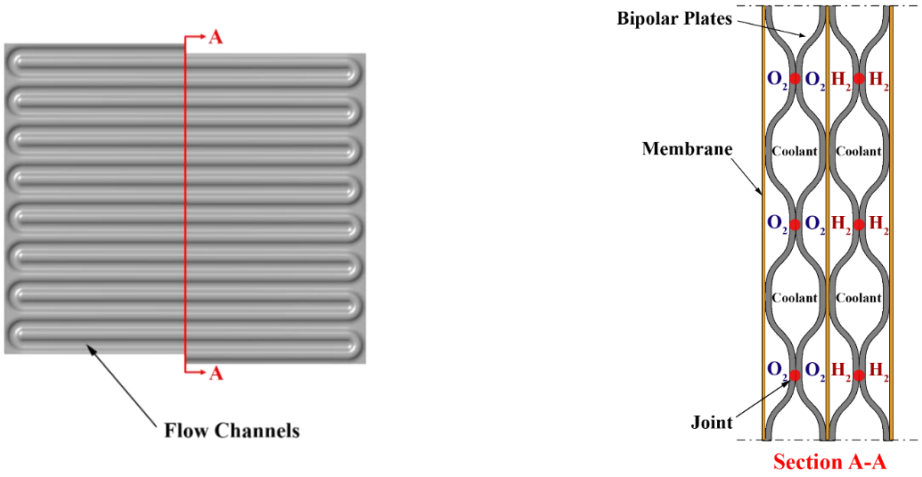

Figure 1.2. *Structure of a bipolar plate, (a) Top view, (b) Cross Section A-A.*

Bipolar plates have an important role on fuel cell stacks. They provide structural support for the mechanically weak membranes, manage the supply of reactant gases through flow channels (see ***Figure 1.2***), improve heat management with a coolant and electrically connect two cells together in the stack [4].

The configuration presented in Figure 1.2 consists of two metallic plates welded together creating the bipolar plate. This configuration repeats along the stack. The reactants flow on one side of the plate, while the cooling fluid flows on the other side of the same plate to remove the heat generated by the chemical reaction [5].

The main material used for bipolar plates is graphite [6]. It offers good electrical conductivity, high corrosion resistance and low interfacial contact resistance. However, the cost of graphite plates is high due to their poor manufacturability and it has the disadvantage of being brittle and having poor permeability which forces the use of thicker plates. In order to decrease the cost of fuel cells, metallic bipolar plates have received much attention lately due to the much superior manufacturability, higher mechanical strength, being non permeable and more durable when submitted to shock and vibration which is important when used for portable applications and transport [4].

The main handicap on metallic plates is the corrosion which occurs in the acidic and humid environment present in a fuel cell. Some solutions for preventing metal degradation consist on using noble metals, stainless steels, aluminium alloys, titanium and nickels as base metal and coating materials to prevent the corrosion on the base metal. Cost wise, stainless steel is promising along with the correct coating [7].

2 NUMERICAL MODEL

The main objective of this paper is to optimize the flow channel geometry with a finite element model. The results obtained can vary depending on the finite element code and boundary conditions as well as the influence of the material used.

2.1 FINITE ELEMENT CODE

The numerical simulations presented in this study were carried out with the in-house finite element code DD3IMP[1] [8], which was specifically developed for sheet metal forming simulation. Regarding its formulation, an updated Lagrangian scheme is used to describe the evolution of the deformation. In each increment, an explicit approach is used to obtain a trial solution for the nodal displacements and then Newton-Raphson algorithm is used to correct the first trial solution, which finishes when a satisfactory equilibrium state is achieved. This is repeated until the end of the process. The Newton-Raphson algorithm is used to solve both the non-linearities associated with the frictional contact and the elastoplastic behaviour of the deformable body in a single iterative loop [9]. In sheet metal forming processes, the boundary conditions are defined by the contact established between the metallic sheet and the forming tools. The friction contact is defined by Coulomb's classical law and the friction coefficient is set as 0.1 for the present paper.

The forming tools are considered perfectly rigid in the numerical model, thus only their exterior surface are described in the numerical model. In this paper the tool's surface is discretized with

[1] DD3IMP – Contraction of "Deep Drawing 3D IMPlicite finite element code" [8]

quadrilateral elements and is then smoothed with Nagata patches [10].
The discretization of the blank was carried out with isoparametric 8-node hexahedral finite elements associated with a selective reduced integration [8][11].

2.2 BOUNDARY CONDITIONS

The proper use of boundary conditions is fundamental to get accurate results in the numerical simulations. In fact, a body unrestrained with applied load presents infinite displacements. In this paper, the boundary conditions were set to represent as close as possible the stamping process. Besides, in order to avoid excessive computational costs, only specific zones of the bipolar plate were analysed. Accordingly, the boundary conditions had to be adapted in order to represent the correct conditions of the selected representative zones looking for symmetries, which allow a portion of the structure to be analysed.

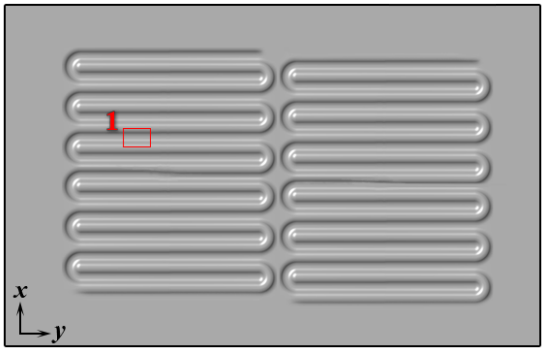

Figure 2.1. *Representation of a serpentine flow field indicating the selected zones analysed.*

Figure 2.1 indicates the different representative zones selected in this study for a serpentine flow field. Each representative zone aims to study a different region of the bipolar plate.
The representative zone number 1 represents half a channel (see Figure 2.2). Adequate boundary conditions are required to represent the symmetry of the channel. Thus, the red plane and its parallel plane on the other extremity represent the constrain in the *x* direction. In the same way, the blue plane and its parallel plane on the other extremity constrain in the *y* direction (plane strain deformation). These conditions were chosen since channels display symmetric geometry and load. These boundary conditions represent the most unfavourable conditions for the stamping process, since they constrain the material flow into the cavity.

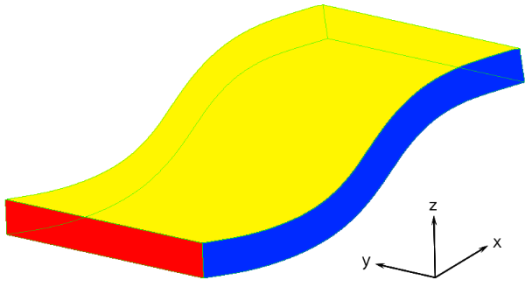

Figure 2.2. *Representation of the boundary conditions for section 1.*

2.3 MATERIAL

The material used for the stamping process of metallic bipolar plates has a large influence on the manufacturing process. In the present paper, the Swift's hardening law (see equation 2.1)) is applied to stainless steel considering an isotropic behaviour (von Mises).

$$Y = \mathrm{K}(\varepsilon_0 - \bar{\varepsilon}^{\mathrm{p}})^n \qquad (2.1)$$

The stainless steel SS 304 is used in this paper and is described with an equation in function of the blank's initial thickness [12]. Swift's hardening law and elastic properties for SS 304 with a blank's initial thickness of 0.1 mm is shown in *Table 2.1*.

Table 2.1. *Swift's hardening law parameters and elastic properties for stainless steel SS 304 with a blank's initial thickness of 0.1 mm.*

	E (GPa)	ν	Y_0 (MPa)	K (MPa)	n
SS 304	162.5	0.30	192.2	850.68	0.206

To apply Swift's hardening law to stainless steels, some aspects have to be taken into account. When stainless steel reaches the plastic domain, microstructural changes trigger changes of mechanical properties. A phase transformation from austenite to martensite can occur which induces simulation errors when applying Swift's hardening law. Studies found that while maintaining low strain rates, the volume fraction of martensite is decreased [13].
Simulations applying Swift's hardening law to stainless steel in this paper are acceptable if the simulations represent low strain rates in the stamping process of the metallic bipolar plates.

3 PARAMETRIC MODEL

To study the influence of multiple geometrical parameters, creating a parametric model simplifies the process of creating the tools' geometry for different studies.

3.1 CHANNEL DIMENSIONS AND FINITE ELEMENT MESH

Every channel dimension is exported from a CAD program (CATIA® V5) to an Excel file in order to change the geometry for different configurations.
Most metallic bipolar plates use a geometry similar with Figure 3.1 with a draft angle, α, applied and only one fillet radius.

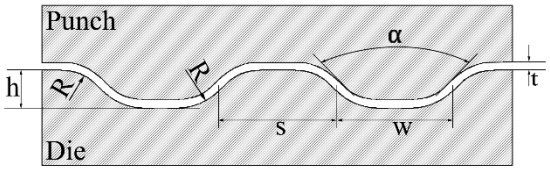

Figure 3.1. *Representation of tool's dimensions.*

This study focuses on the study of an optimized geometry where a second fillet radius is introduced and the draft angle, as a variable, disappears. This geometry is shown in Figure 3.2.
Seven parameters can be changed from the Excel file: channel depth, *h*, channel width, *w*, Rib width, *s*, Blank's initial thickness, *t*, fillet radius, *R*, main radius, *r* and flat section, *a*.
The channel dimensions are set on a mid-plane between the punch and the die to guarantee the symmetry of the geometry. The tool's dimensions are then obtained with an offset from the mid-plan.

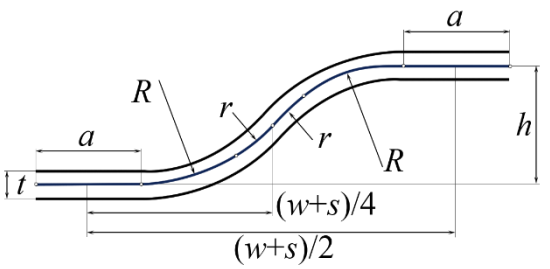

Figure 3.2. *Parametric model.*

For the study on this paper, the main geometrical parameters will vary between a range of values described in Table 3.1 with its respective increment.

Table 3.1. *Range of values for the study of geometrical parameters and their respective increments.*

	Minimum Value [mm]	Maximum Value [mm]	Increment [mm]
w	1.2	2.4	0.05
s	1.2	2.4	0.20
h	0.3	0.65	0.05
R	0.8	1.5	0.10
r	0.2	0.55	0.05
a	0.2	0.6	0.05

The process consists on creating the tool's surface geometry with a CAD program and export in an IGES format for further meshing with the pre-processing program GID® and smoothed with Nagata patches' quadratic interpolation. The final smoothed tool's mesh is shown in Figure 3.3.

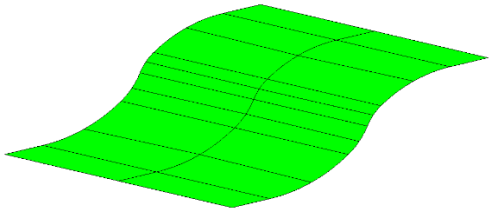

Figure 3.3. *Mesh representation for the die.*

The tools can then be exported to the finite element code DD3IMP for further simulation. The mesh of the blank is generated using a single finite element along the width (plane strain deformation) and four finite elements along the thickness. The number of finite elements along the blank's length will be updated to maintain quadratic elements as square as possible.
After the process of creating a parametric model and the finite element mesh, simulations are ready to proceed.

4 INFLUENCE OF GEOMETRICAL PARAMETERS

A microstamping process is replicated for this study. The process is divided in two phases: first the dies is maintained stationary while the punch moves towards the blank to form the desired shape. This phase ends when the distance between both tools is equal to the blank's initial thickness. The second and final phase is the removal of both tools in a single instant for the springback effect to occur.

The thickness reduction on the stainless steel blank is studied as principal parameter to evaluate the formability of the channel.

4.1 INFLUENCE OF CHANNEL DEPTH, *h*

To evaluate the influence of the channel depth on the formability, the remaining parameters are unchanged and shown in Table 4.1. The channel depth starts with 0.3 mm and using an increment of 0.05 mm for each geometry until the thickness reduction reaches over 30%. In this case, the range is between 0.3 mm and 0.65 mm, which corresponds to the geometry of the die shown in Figure 4.1 and Figure 4.2, respectively.

Table 4.1. *Tool's geometrical dimensions for the study on the channel depth (SS 304).*

***w, s* [mm]**	***r* [mm]**	***h* [mm]**
1.2	0.5	0.3 – 0.65
***R* [mm]**	**a [mm]**	
1.3	0.2	

Figure 4.1. *Die geometry for h = 0.3 mm.*

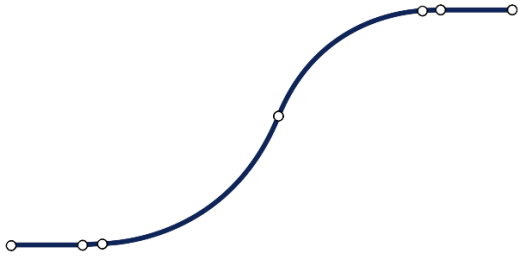

Figure 4.2. *Die geometry for h = 0.65 mm.*

The evolution of the thickness reduction along the blank is shown in Figure 4.3

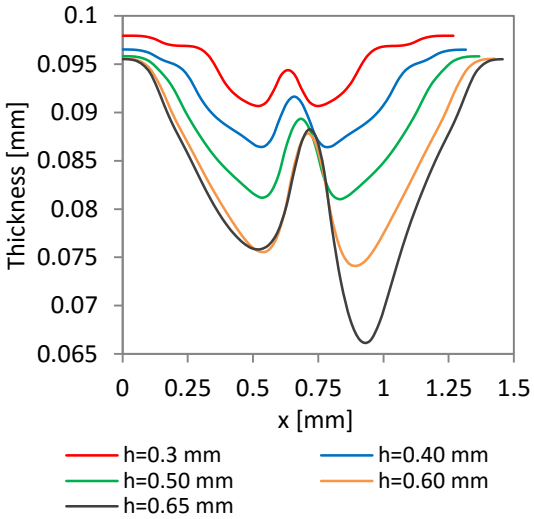

Figure 4.3. *Influence of channel depth on the final thickness.*

A channel depth of 0.65 mm induces a thickness reduction of over 30% as shown in Figure 4.3. With a channel depth of 0.3 mm the maximum thickness reduction is under 10% and with a channel depth of 0.65 mm the thickness reduction is over 30%. The maximum value of thickness reduction increases quadratically with the channel depth. The punch force is shown in Figure 4.4. and increases as the channel depth increases Until approximately 0.15 mm of punch displacement, the force evolution is coincident for all the geometries analysed.

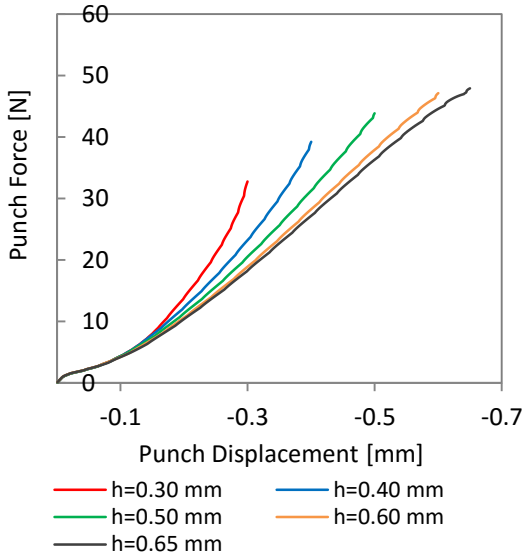

Figure 4.4. *Influence of channel depth on the punch force.*

4.2 INFLUENCE OF THE FILLET RADIUS, *R* and *r*.

In order to evaluate the influence of the fillet radius on the formability, the remaining parameters are set as shown in *Table 4.2*. The fillet radius starts

with 0.8 mm due to the geometry constraints, using an increment of 0.1 mm for each geometry until the evolution on the formability stabilises. In this case, the range is between 0.8 mm and 1.5 mm, which corresponds to the geometry of the die shown in Figure 4.5 and Figure 4.6, respectively

Table 4.2. *Tool's geometrical dimensions for the study on the fillet radius (SS 304).*

***w, s* [mm]**	***r* [mm]**	***h* [mm]**
1.2	0.5	0.4
***R* [mm]**	**a [mm]**	
0.8 – 1.5	0.2	

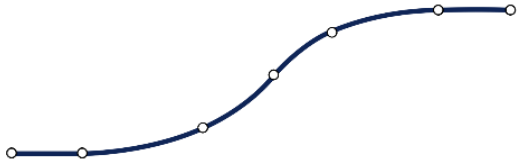

Figure 4.5. *Die geometry for R = 0.8 mm*

Figure 4.6. *Die geometry for R = 1.5 mm*

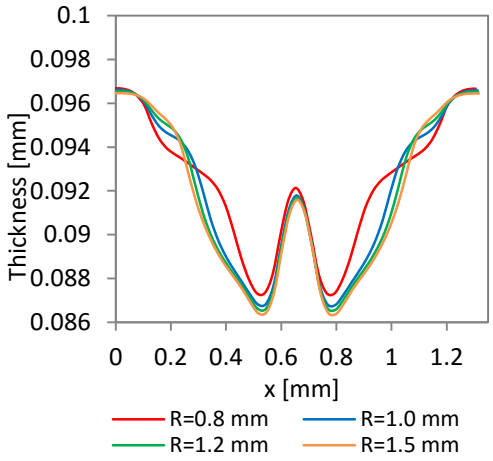

Figure 4.7. *Influence of the fillet radius on thickness reduction.*

The thickness distribution along the blank is shown in Figure 4.7.

The geometry for a fillet radius of 1.5 mm tends to work as an extended flat section with only one fillet radius demonstrating inferior results in terms of formability. With a fillet radius of 0.8 mm the maximum thickness reduction is 12.7% and with a fillet radius of 1.5 mm the thickness reduction is over 13.6%. The value of the maximum thickness reduction increases with a quadratic tendency.

To evaluate the influence of the main radius on the formability, the remaining parameters are set as shown in Table 4.3. The main radius starts with 0.55 mm due to the geometry constraints, using an increment of 0.05 mm for each simulation until 30% thickness reduction is obtained. Thus, the range is between 0.2 mm and 0.55 mm, which corresponds to the geometry of the die shown in Figure 4.8 and Figure 4.9, respectively.

Table 4.3. *Tool's geometrical dimensions for the study on the main radius (SS 304).*

***w, s* [mm]**	***r* [mm]**	***h* [mm]**
1.2	0.2 – 0.55	0.4
***R* [mm]**	**a [mm]**	
1.3	0.2	

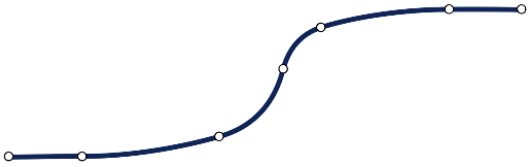

Figure 4.8. *Die geometry for r = 0.2 mm.*

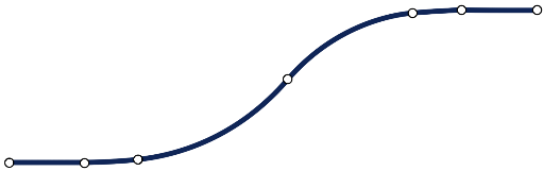

Figure 4.9. *Die geometry for r = 0.55 mm.*

With a main radius of 0.2 mm the maximum thickness reduction is over 28% and with a main radius of 0.5 mm the thickness reduction is under 15%. Increasing the main radius decreases the thickness reduction with a quadratic tendency as shown in Figure 4.10. The geometry for a main radius of 0.55 mm is smoother than for a main radius of 0.2 mm explaining the increase in formability for higher values of the main radius. The comparison between Figure 4.7 and Figure 4.10 allows to conclude that the impact of the main radius is significantly higher than the fillet radius.

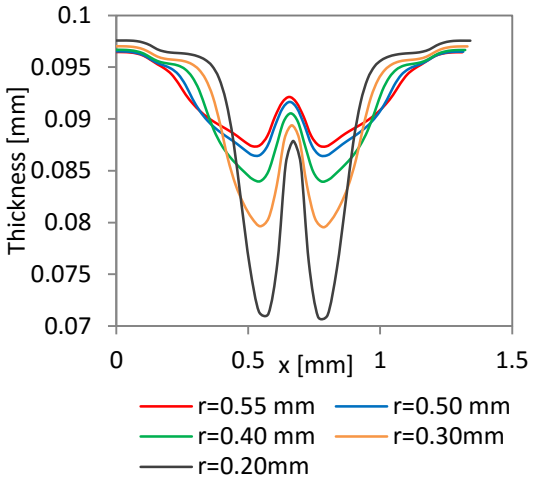

Figure 4.10. *Influence of the main radius on the thickness reduction.*

4.3 INFLUENCE OF THE CHANNEL WIDTH, RIB WIDTH AND FLAT SECTION, w, s, a.

To evaluate the influence of the channel and rib width on the formability, the remaining parameters are set as shown in *Table 4.4*.

Table 4.4. *Tool's geometrical dimensions for the study on the channel and rib width (SS 304).*

***w, s* [mm]**	***r* [mm]**	***h* [mm]**
1.2 – 2.4	0.3	0.5
***R* [mm]**	**a [mm]**	
1.3	0.2 – 1.4	

The channel and rib width start with 1.2 mm and increased with an increment of 0.2 mm until a tendency can be observed. Since the objective is to study the influence of the plane section, the value of the flat section, *a*, must also be increased accordingly with the same increment as the channel and rib dimensions. In this case, the range if the channel and rib width is between 1.2 mm and 3.4 mm and the range for the flat section is between 0.2 mm and 2.4 mm. The geometry of the die for these values is shown in Figure 4.11.

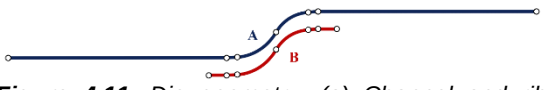

Figure 4.11. *Die geometry: (a) Channel and rib width of 3.4 mm, (b) Channel and rib width of 1.2 mm.*

The thickness reduction for different channel and rib width presents a quadratic decreasing tendency with the increase of these parameters as shown in Figure 4.12 and it is expected to tend to no thickness reduction for an infinite channel and rib width. The increase in formability was expected due to the increase in material available to flow into the cavity and form the channel. With a channel and rib width of 1.2 mm the maximum thickness reduction is 19% and with a channel and rib width of 3.4 mm the thickness reduction is under 12%.

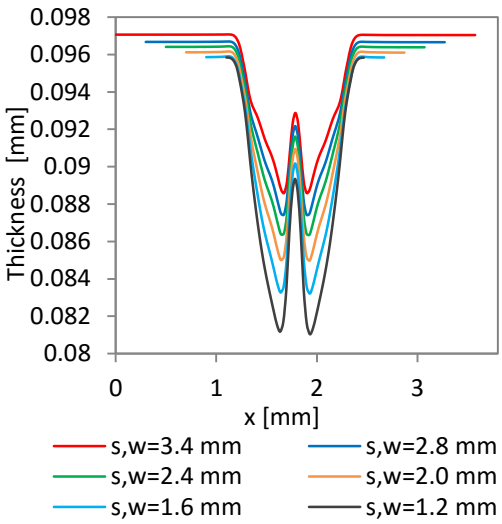

Figure 4.12. *Influence of the channel and rib width on the thickness reduction.*

In order to evaluate the influence of the flat section on the formability, the remaining parameters are set as shown in *Table 4.5*. The flat section starts with 0.2 mm and is increased with an increment of 0.05 mm until the geometry itself prevents further increments. In this case, the range is between 0.2 mm and 0.6 mm and the geometry of the die for these values is shown in Figure 4.13 and Figure 4.14.

Table 4.5. *Tool's geometrical dimensions for the study of the flat section (SS 304).*

***w, s* [mm]**	***r* [mm]**	***h* [mm]**
1.2	0.5	0.4
***R* [mm]**	**a [mm]**	
1.3	0.2 – 0.6	

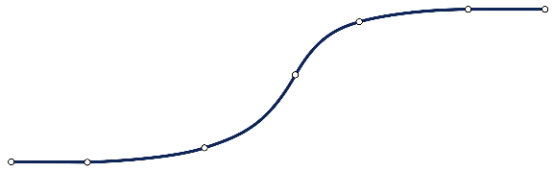

Figure 4.13. *Die geometry for a = 0.2 mm.*

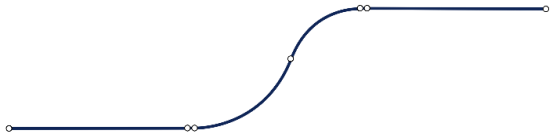

Figure 4.14. *Die geometry for a = 0.6 mm.*

5 CONCLUSIONS

The formability of a metallic bipolar plate was studied in this paper for a microstamping process. The influence of the geometrical parameters was tested to consider the dimensions which increase

the formability of the blank. Six parameters were tested:

- The first parameter to be tested was the channel depth, h. The thickness reduction increased with the increase of the channel depth. The maximum value of thickness reduction followed a quadratic crescent tendency as the channel depth was increased. It was possible to reach a channel depth of 0.65 mm with a maximum thickness reduction of 30%. The increase in channel depth led to an increase in punch force.
- The second parameter was the added fillet radius, R. The thickness reduction increased with the increase of the fillet radius. Once again, observing the maximum thickness reduction for each simulation, it was clear that it followed a quadratic crescent tendency as the fillet radius increased. The best results were observed for an added fillet radius of 0.8 mm which corresponds to a maximum thickness reduction of 12.7%. The main fillet radius, r, was also studied. When the main fillet radius increased, the thickness reduction decreased with a quadratic tendency. The best results were observed for a main fillet radius of 0.5 mm (maximum thickness reduction under 15%).
- The next parameter studied was a plane section of the cross-section of the straight channel. To evaluate such section, both the rib, s, and channel width, s, were increased to maintain the symmetry, as well as the flat section, a. With the straight section increased, the maximum thickness reduction decreased with a quadratic tendency.
- In order to keep the channel and rib width, the next parameter analysed was the flat section, a. Increasing this parameter without altering the channel and rib width, the arc length of the fillet radius changed, reducing the formability of the blank. Increasing the flat section to 0.6 mm induced a maximum thickness reduction of 23.7%.

6 REFERENCES

[1] L. Carrette, K. a Friedrich, and U. Stimming, “Fuel Cells - Fundamentals and Applications,” *Fuel Cells*, vol. 1, no. 1, pp. 5–39, 2001.

[2] S. Mahabunphachai, Ö. Necati, and M. Koc, “Effect of manufacturing processes on formability and surface topography of proton exchange membrane fuel cell metallic bipolar plates,” vol. 195, pp. 5269–5277, 2010.

[3] Y. Wang, K. S. Chen, J. Mishler, S. C. Cho, and X. C. Adroher, “A review of polymer electrolyte membrane fuel cells: Technology, applications, and needs on fundamental research,” *Appl. Energy*, vol. 88, no. 4, pp. 981–1007, 2011.

[4] L. Peng, P. Yi, and X. Lai, “Design and manufacturing of stainless steel bipolar plates for proton exchange membrane fuel cells,” *Int. J. Hydrogen Energy*, vol. 39, no. 36, pp. 21127–21153, 2014.

[5] X. Li and I. Sabir, “Review of bipolar plates in PEM fuel cells: Flow-field designs,” *Int. J. Hydrogen Energy*, vol. 30, no. 4, pp. 359–371, 2005.

[6] W. Yoon, X. Huang, P. Fazzino, K. L. Reifsnider, and M. A. Akkaoui, “Evaluation of coated metallic bipolar plates for polymer electrolyte membrane fuel cells,” *J. Power Sources*, vol. 179, no. 1, pp. 265–273, Apr. 2008.

[7] H. Tawfik, Y. Hung, and D. Mahajan, “Metal bipolar plates for PEM fuel cell-A review,” *J. Power Sources*, vol. 163, no. 2, pp. 755–767, 2007.

[8] L. F. Menezes and C. Teodosiu, “Three-dimensional numerical simulation of the deep-drawing process using solid finite elements,” *J. Mater. Process. Technol.*, vol. 97, no. 1–3, pp. 100–106, 2000.

[9] M. OLIVEIRA, J. ALVES, B. CHAPARRO, and L. MENEZES, “Study on the influence of work-hardening modeling in springback prediction,” *Int. J. Plast.*, vol. 23, no. 3, pp. 516–543, Mar. 2007.

[10] D. M. Neto, M. C. Oliveira, L. F. Menezes, and J. L. Alves, “Applying Nagata patches to smooth discretized surfaces used in 3D frictional contact problems,” *Comput. Methods Appl. Mech. Eng.*, vol. 271, pp. 296–320, 2014.

[11] T. J. R. Hughes, “Generalization of selective integration procedures to anisotropic and nonlinear media,” *Int. J. Numer. Methods Eng.*, vol. 15, no. 9, pp. 1413–1418, Sep. 1980.

[12] Y. Liu and L. Hua, “Fabrication of metallic bipolar plate for proton exchange membrane fuel cells by rubber pad forming,” *J. Power Sources*, vol. 195, no. 11, pp. 3529–3535, 2010.

[13] S. Msolli, M. Martiny, M. C. Cardoso, L. P. Moreira, S. Mercier, and A. Molinari, “Numerical modeling of the deformation of AISI 304L using a tangent additive Mori-Tanaka homogenization scheme: Application to sheet metal forming,” *J.*

Mater. Process. Technol., vol. 235, pp. 187–205, 2016.